Geological Society of America
3300 Penrose Place
P.O. Box 9140
Boulder, CO 80301
(303) 447-2020 • fax 303-357-1073
www.geosociety.org

Geological Society of America
Special Paper 384
2005

Geochemistry of target rocks, impact-melt particles, and metallic spherules from Meteor Crater, Arizona: Empirical evidence on the impact process

David W. Mittlefehldt*
Friedrich Hörz
SR, National Aeronautics and Space Administration Johnson Space Center, Houston, Texas 77058, USA

Thomas H. See
C23, Lockheed Martin SO, 2400 Nasa Road 1, Houston, Texas 77058, USA

Edward R.D. Scott
Hawai'i Institute of Geophysics and Planetology, University of Hawai'i, Honolulu, Hawai'i 96822, USA

Stanley A. Mertzman
Department of Geosciences, Franklin & Marshall College, Lancaster, Pennsylvania 17604, USA

ABSTRACT

We have done lithophile- and siderophile-element analyses of a large suite of target rocks, ballistically dispersed impact-melt particles and ballistically dispersed metallic spherules from Meteor Crater, Arizona. The Moenkopi Formation (topmost unit) has a unique lithophile-element signature that confirms it as a major component of the impact-melt particles. The Kaibab Formation is very heterogeneous, containing dolomite-rich and quartz-rich layers. The lithophile-element compositions of the impact-melt particles can be entirely explained as mixtures of Moenkopi and Kaibab depleted in CO_2. The Toroweap and Coconino Formations (lowest units) are not required components, but small contributions from them cannot be excluded. We conclude the impact-melt particles were formed entirely in the upper portion of the section, above the lower two units.

The impact-melt particles average ~14 wt% projectile material. Most siderophile-element ratios of the impact-melt particles are unchanged from those of the projectile. Many samples are depleted in Au; the most extreme depletions are in impact-melt particles with the highest Kaibab component. Kaibab rocks are highest in Br, and we suggest loss of volatile Au halides may have caused the fractionation.

Ballistically dispersed metallic spherules are enriched in Co, Ni, Ir, and Au compared to Canyon Diablo metal. Element/Ni ratios deviate slightly from projectile ratios, and are inversely correlated with susceptibility to oxidation relative to Ni. We attribute this to partial oxidation of molten metal spherules during flight. Spherule compositions suggest some selective melting of graphite-troilite-schreibersite inclusions of the projectile, consistent with enhanced shock melting of these lower density phases.

Keywords: Meteor Crater, Arizona, impact-melt particles, geochemistry, target rocks, siderophile elements, projectile-target mixing

*Corresponding author: david.w.mittlefehldt@nasa.gov

Mittlefehldt, D.W., Hörz, F., See, T.H., Scott, E.R.D, and Mertzman, S.A., 2005, Geochemistry of target rocks, impact-melt particles, and metallic spherules from Meteor Crater, Arizona: Empirical evidence on the impact process, *in* Kenkmann, T., Hörz, F., and Deutsch, A., eds., Large meteorite impacts III: Geological Society of America Special Paper 384, p. 367–390.

"Special features, such as the presence of layering or volatiles in the target are not shown here. The effects of such circumstances are largely unknown at present."

—H.J. Melosh, *Impact Cratering: A Geologic Process,* p. 48

INTRODUCTION

The study of impact processes has progressed along a five-pronged front: (*i*) field and petrologic study of terrestrial impact craters and their products; (*ii*) laboratory-scale impact experiments; (*iii*) large-scale explosion experiments; (*iv*) theoretical modeling of the impact process; and (*v*) astronomical and spacecraft study of craters on planets, moons and asteroids (see Melosh, 1989). Geochemical studies have contributed to the identification of meteoritic signatures in impact melts (e.g., King et al., 2002), attempted to identify the type of impactor (Morgan et al., 1975; Palme, 1982; Palme et al., 1978), or established the process of mixing of target rocks to form unusual impact-melt rocks (e.g., Dence, 1971; Grieve, 1982; Simonds et al., 1978). Chemical studies aimed at a more detailed understanding of the cratering process have been limited for several reasons. Older structures have been eroded and/or buried, making detailed reconstruction of the pre-impact chemical stratigraphy difficult. Impact-melt sheets in larger structures may have suffered hydrothermal alteration (see Hagerty and Newsom, 2003), which affected the composition of the melt sheet. Finally, older and larger structures do not have preserved meteoritic material available for study (Grieve, 1991), precluding unambiguous identification of the impactor. As a consequence, the depth of the melt zone is poorly defined, and little is known regarding fractionation of impactor and target rocks during melting.

A few younger, smaller impact craters with preserved projectile material have been studied. Attrep et al. (1991) did geochemical studies of a few samples from Henbury and Wolfe Creek Craters. These authors showed that siderophile-element ratios in "impactites" are fractionated relative to those of the preserved projectile material. We did an extensive study of samples from Wabar Crater that confirmed that siderophile-element fractionations occurred during formation of impact-glass particles (Mittlefehldt et al., 1992). We suggested that because lithophile elements were not fractionated in the glasses, the siderophile-element fractionation must have occurred before mixing of projectile and target materials. We also inferred that projectile material was preferentially mixed with the upper stratigraphic horizons of the target.

We have continued our study of natural impacts through field, petrologic, and geochemical studies of Meteor Crater, Arizona, the largest crater with preserved projectile material (Grieve, 1991). Meteor Crater is almost ideal for this study. The stratigraphy is variegated, allowing a more detailed look at the projectile-target interaction; it is young and fresh; abundant impact-melt materials already reside in collections; and remnants of the projectile have been well characterized. The results of our detailed study of the mineralogy and major-element chemistry of the target rocks and the petrology of the impact glasses have been reported (Hörz et al., 2002; See et al., 2002). Here we present our completed study of lithophile and siderophile elements for target rocks, impact-melt particles, and metallic spherules.

GEOLOGIC SETTING AND BACKGROUND

Target Rocks

Meteor Crater is one of the best-studied terrestrial impact structures. The synopsis given here is taken from Roddy (1978), Roddy et al. (1975) and Shoemaker (1963; 1987). See et al. (2002) presented details of the major-element chemistry and mineralogy of a stratigraphic sequence systematically collected from the crater walls.

Meteor Crater was formed in a sequence of flat-lying Mesozoic and Paleozoic sediments. The uppermost unit, the Triassic Moenkopi Formation, consists of calcareous sandstone and siltstone, estimated to have averaged ~8.5 m in thickness in the target area (Roddy, 1978). The Moenkopi is more carbonate-rich at the top and more quartz-rich at the bottom (See et al., 2002). Below the Moenkopi is the Permian Kaibab Formation, an ~80 m thick carbonate sequence consisting largely of sandy dolomite, but including some sandstone. The composition of this unit is highly variable, reflecting wide ranges in quartz and dolomite content; calcite is a minor component. The upper half of the unit is richer in carbonate than is the lower half (See et al., 2002). Below the Kaibab is the ~1.5 m thick Toroweap Formation consisting dominantly of dolomitic sandstone. The crater bottoms in the ~220 m thick Coconino Formation of very pure sandstone (Kieffer, 1971). Below the Coconino is the Permian Supai Formation of sandstone and siltstone. There is no evidence that the transient crater excavated this formation.

Canyon Diablo Iron Meteorite

The projectile was the Canyon Diablo IAB iron meteorite, estimated to have been ~33 m in diameter for an assumed impact velocity of 15 km/sec (Roddy, 1978). The IAB irons, especially Canyon Diablo, have been extensively studied. Wasson and Ouyang (1990) have done a detailed compositional study of Canyon Diablo, while Choi et al. (1995) have presented a thorough study of the composition of the metal phase of most IAB irons. Choi et al. (1995) present an average composition of Canyon Diablo metal which we use for our discussions (Appendix 1). The composition of the Canyon Diablo iron, with 70 mg/g Ni, is typical of that of the majority of IAB irons (Choi et al., 1995).

Buchwald (1975) gave a detailed description of the petrology of Canyon Diablo. It is a coarse octahedrite containing ~8.5% by volume of graphite-troilite inclusions. These inclusions have varying ratios of troilite to graphite, but Buchwald (1975) estimated that on average, they have roughly equal amounts of troilite and graphite by volume. The inclusions are typically surrounded

by schreibersite and cohenite (Benedix et al., 2000; Buchwald, 1975). Silicate inclusions are present in many members of the IAB group and are mostly chondritic in composition (e.g., Benedix et al., 2000; Bunch et al., 1970; Mittlefehldt et al., 1998). Buchwald (1975) reported that rare silicates are present in some graphite-troilite nodules in Canyon Diablo.

Meteor Crater and Impact Products

Meteor Crater is a bowl-shaped impact crater ~1 km in diameter. Structural controls in the target rocks give it a squarish shape in map view (Roddy, 1978). The crater was formed ~50 k.y. ago (Nishiizumi et al., 1991; Phillips et al., 1991). Shocked and frothy Coconino sandstone occurs in the crater floor below a layer of alluvium, but no continuous impact-melt sheet is present (Roddy et al., 1975). Shocked and brecciated target rock occurs on the crater floor, in the walls and in the overturned flap (Roddy et al., 1975). Impact melt composed of mixtures of target rock and projectile are confined to particles up to a few cm in size ballistically dispersed over the surrounding plains (Nininger, 1956). Metallic spherules a few mm in diameter are also found on the surrounding plains (Nininger, 1956). These are melt-droplets of the Canyon Diablo iron and are not mixed with target rock (Blau et al., 1973). Some samples of Canyon Diablo show petrographic evidence for shock deformation superimposed on the normal structure of the iron. These are solid fragments of the impactor spalled from the backside of the projectile as the shock wave reflected off the free surface (Buchwald, 1975).

SAMPLES AND ANALYTICAL METHODS

Samples

We have analyzed three types of materials for this study: (*i*) representative samples of target rocks, mostly from within the crater or the overturned flap, (*ii*) ballistically dispersed impact-melt particles, and (*iii*) ballistically dispersed metallic spherules. A few of the target-rock samples analyzed early on are representative hand samples of the Kaibab and Coconino Formations, but are from undocumented locations. A set of documented samples from the crater was collected to obtain a representative suite of target rocks; these are briefly described in Appendix 2. A final set of samples was collected to obtain a continuous stratigraphic sequence from within the crater for geochemical and mineralogical characterization. Major-element analyses by X-ray fluorescence (XRF), and mineralogy determined by X-ray diffraction (XRD) of these samples are given in See et al. (2002). The impact-melt particle and metallic spherule samples were obtained from the collection of the Center for Meteorite Studies, Arizona State University. H.H. Nininger collected these samples from the plains surrounding the crater, but their precise collection locations are not known. The impact-melt particles were selected by one of us (FH) to represent the range of materials in the collection. Brief macroscopic descriptions of these are given in Appendix 3. The petrology of the impact-melt particles has been discussed in detail in Hörz et al. (2002).

Analytical Methods

The target-rock and impact-melt particle samples were analyzed by instrumental neutron activation analysis (INAA) at Johnson Space Center (JSC) in a series of irradiations. The target rocks labeled Ma, Ka, Ta, Ca, etc., are splits of the pooled subsection samples of See et al. (2002). For the other target rocks, several grams of each sample were ground and homogenized, and splits taken for analysis. Some of the impact-melt particles contained variable amounts of adhering alteration material, or fine-grained soil particles. These contaminants were removed by scraping with a dental pick and ultrasonication in distilled water. The impact-melt particles were coarsely crushed and the cleanest material was handpicked. Many of the impact-melt particles are finely vesicular, and alteration material was found even in interior vesicles. (It is possible that the alteration phases in interior vesicles represent material mobilized during quenching and cooling of the particles, and not later, secondary alteration phases.) It proved impossible to eliminate all alteration material. The occurrence of alteration material in tiny interior vesicles indicates that it likely formed from elements leached out of the glass. Samples of alteration material from three impact-melt particles were analyzed in order to evaluate the potential effects of this material on analyses. For large impact-melt particles, clean material was crushed and homogenized and splits taken for INAA. For small particles, the entire clean sample was used for INAA.

Samples, standards, and international standard rocks used as controls were sealed in ultra-pure silica glass tubes, and irradiated at the University of Missouri Research Reactor Facility. The samples were counted several times after irradiation to obtain data for nuclides of differing half-lives. Irradiation times, neutron fluxes, and counting schedules were slightly different for the different irradiations. Data reduction was done using standard JSC procedures (Mittlefehldt and Lindstrom, 1991, 1993). The impact-melt particles and some target rocks have high Mg and low Na contents. A correction to the data was applied to account for Na produced by (n,p) reactions on Mg. The ultra-pure silica contains a tiny amount of La that can significantly affect the data for very low La samples. A blank correction was made when needed.

The metallic spherules were analyzed by INAA at the University of California at Los Angeles (UCLA) in the mid 1970s. The samples consisted of metal cores with oxide coatings. Following Kelly et al. (1974), the samples were abraded in a mixer-mill with a sandpaper lining until the oxide coatings appeared to have been removed. The spherule samples, six samples of the North Chile hexahedrite (IIA iron) Tocopilla serving as standards, and the IVA iron meteorite Rembang serving as a control, were irradiated at the Ames Laboratory Research Reactor at a flux of 2×10^{13} n cm^{-2} sec^{-1} for 10 h, and counted several times to obtain data for elements of differing half-lives. Subsequently, four of the samples were reirradiated

at the UCLA reactor for radiochemical determination of Ga and Ge following the procedures of Wasson and Kimberlin (1967).

Splits of the larger impact-melt particles were powdered and fused to glass on a Mo metal strip in an Ar atmosphere (Brown, 1977) for major element analysis by electron microprobe (EMPA). We experienced two problems using this procedure. First, the impact-melt particles are not in internal equilibrium, especially with respect to oxidation state—they contain Fe^{3+}, Fe^{2+}, and Fe^{0} (Hörz et al., 2002). This caused some oxidation of Mo which dissolved in the glass at up to a few wt%. Second, some of the Fe remained in the metallic state, and was not part of the homogeneous glass. Thus, there is poor agreement between FeO determined by INAA and EMPA. However, major-element data are only used to determine which of the target rocks (all Fe-poor) contributed to the impact-melts. Most of the Fe in the impact-melt particles is derived from the impactor (See et al., 2002; this study). To first order, FeO can be ignored in evaluating target-rock contributions to the impact-melt particles. The glass beads were analyzed with the JSC SX100 electron microprobe using a 15 kV potential, 15 nA sample current, and the electron beam rastered over a 10 × 10 μm area.

See et al. (2002) presented major-element analyses by XRF of many of the target rocks studied here. Additional target-rock samples plus a composite of 15 impact-melt particles were analyzed as part of this study. The analytical methods follow standard procedures used at Franklin & Marshall College, described in detail by Boyd and Mertzman (1987) and Mertzman (2000). An exception to these procedures is that the samples were first ground and homogenized in an agate mortar and pestle at JSC, and splits sent to Franklin & Marshall College for analysis. Final grinding and sieving were done at Franklin & Marshall. Major-element contents were determined by XRF analysis, with all Fe determined as Fe_2O_3. The ferrous iron content was determined by titration, and loss on ignition was determined by heating an aliquot at 950 °C for one hour.

RESULTS

Table 1 presents the major-element analyses of the target rocks plus the composite impact-melt particle (H11; see Appendix 3). The XRF analysis determines major elements on a volatile-free basis, and all Fe as Fe_2O_3. In Table 1, the data have been recast to a volatile-bearing basis, and with Fe split between FeO and Fe_2O_3 as determined by titration. The low sum quoted for the composite impact-melt particle is an artifact of the recalculation—the XRF sum was 99.31. The INAA data on target rocks, including those studied by See et al. (2002) are given in Table 2. Our INAA data on impact-melt particles are given in Table 3, and major-element analyses of select impact-melt particles determined by EMPA on fused beads are presented in Table 4. These latter analyses are normalized to 100%. The analyses included variable amounts of MoO_2 (<0.01–4.56 wt%) derived from the strip heater, and the Fe in the glass likely is a mixture of FeO and Fe_2O_3. These analyses are used to evaluate which target rocks dominate in the impact-melt particles, and devolatilized, Fe-free (projectile-free) compositions are used for this. Table 5 contains our INAA data on the ballistically dispersed metallic spherules. We have also done INAA on a few miscellaneous samples from the impact-melt particle suite—a lithic clast, samples of secondary alteration products and an oxide bead. These data are given in Appendix 4 for completeness.

DISCUSSION

Comparing geochemical data on the target rocks with those on impact-melt particles is not straightforward. The high-temperature formation of the impact-melt particles caused devolatilization of carbonates and hydrous phases of the target components, and mixing with projectile material diluted the target components. To overcome these problems, we use normalized compositions. The impact-melt particle compositions are normalized to an Fe-Ni-Co-free basis. The volatile content of these particles is not known, but they should be nearly volatile-free. We use the loss on ignition (LOI) determination on the composite of 15 impact-melt particles (H11, Table 1) to correct for volatile content. The target-rock compositions are normalized to a volatile-free basis using the LOI determinations, and to an iron-free basis to make them directly comparable to the impact-melt particles. These corrected impact-melt and target-rock compositions are referred to as adjusted compositions. The impact-melt particles studied here are bulk particles, including glass, quenched mineral phases, undigested clasts, and remnant metal and sulfide beads, and thus are not directly comparable to the pure glass compositions reported by Hörz et al. (2002).

Geochemical Stratigraphy of Meteor Crater

The upper portion of the target stratigraphy shows substantial major-element compositional heterogeneity (Hörz et al., 2002; See et al., 2002). The Moenkopi Formation shows generally decreasing CaO and LOI, and increasing SiO_2 with depth, indicating increasing sand and decreasing carbonate. The Kaibab exhibits substantial fluctuation in SiO_2 and MgO+CaO throughout the section reflecting variations in quartz and dolomite. On a finer scale, we found that the quartz content of the Kaibab varies from ~100% to ~15% within the section (Hörz et al., 2002; See et al., 2002). These variations are non-systematic—the Kaibab sample with the lowest quartz content is adjacent to a sample with one of the highest (see Hörz et al., 2002; Figure 15; samples K106.2 and K104.7). The Toroweap and Coconino are distinguishable from other target rocks by their high SiO_2 contents.

Variations in adjusted major-element content of the target rocks with depth in the crater are shown in Figure. 1. The Moenkopi is distinct in having much higher Ti and Al contents, while the Kaibab is distinct in having a much higher Mg content, and generally lower but variable Si content. The high Al content of the Moenkopi indicates a higher terrigenous component (clays). This is also seen in Sc, rare-earth elements, and Ta contents

(Fig. 2). The two lowest Moenkopi samples are also rich in Hf, but the upper portion has Hf contents like those of the Kaibab. The Kaibab is distinct in showing a general increase in U content with depth, and the lower portion of the section has the highest U content in the depth profile (Fig. 2).

The Toroweap and Coconino have lower adjusted contents of all major and trace elements, excluding Si (Figs. 1 and 2). Hence, these units would only act as diluents in lithophile-element mixing relations should they be a component of the impact-melt particles. (The Toroweap is a minuscule volume fraction of the section, and could not significantly affect the composition of impact-melt particles.)

Lithophile Elements and Target Rock Mixing

Kargel et al. (1996) suggested that impact-melt particles from Meteor Crater are composed of mixtures of projectile and rock from the Kaibab Formation, with no clear signature for either Moenkopi or Coconino rocks. Our preliminary synopsis of target rock and impact-melt particle compositions led us to suggest that both Moenkopi and Kaibab strata are important terrestrial components of the particles (Mittlefehldt et al., 2000). This was supported by our modeling of the major-element compositions of glasses contained in the impact-melt particles. We identified three distinct melt compositional types and concluded that mixtures of Moenkopi and Kaibab in variable proportions could explain the glasses, with Moenkopi composing as much as half of the target component in some (Hörz et al., 2002). We could not exclude Toroweap or Coconino as minor components of some glasses, however. We suggested that the melt zone was a relatively small fraction of the transient crater volume, and that melting occurred at depths of <30 m for many, and possibly all, of the glasses (Hörz et al., 2002).

Mixing relations for major elements Mg-Al, Ca-Al and Ti-Si between target rocks and bulk impact-melt particles are shown in Figure 3. All impact-melt particles fall between the fields of Moenkopi and Kaibab samples, and none have compositions that would require addition of Toroweap or Coconino into the mix.

TABLE 1. MAJOR-ELEMENT COMPOSITIONS OF TARGET ROCKS AND A COMPOSITE OF SEVERAL IMPACT-MELT PARTICLES DETERMINED BY XRF AND IRON TITRATION.

	Moenkopi		Kaibab					Toroweap
	MC-01	MC-07	K-1	K-2	MC-06	MC-10	MC-12	MC-08
SiO_2	83.94	57.76	14.52	2.41	45.36	35.31	44.12	95.74
TiO_2	0.44	0.49	0.04	0.01	0.12	0.10	0.09	0.08
Al_2O_3	6.95	6.14	0.78	0.13	2.09	2.28	1.48	1.62
Fe_2O_3	0.86	1.58	0.11	0.28	0.19	0.16	0.70	0.00
FeO	0.34	0.14	0.07	0.20	0.07	0.16	0.06	0.11
MnO	0.03	0.06	0.02	0.03	0.04	0.03	0.02	0.00
MgO	0.39	1.44	18.12	20.77	10.60	12.18	10.70	0.03
CaO	2.01	16.05	26.82	30.83	15.60	19.25	16.65	0.54
Na_2O	0.02	0.04	0.07	0.07	0.07	0.06	0.07	0.00
K_2O	1.24	1.17	0.15	0.03	0.44	0.45	0.26	0.46
P_2O_5	0.13	0.13	0.03	0.03	0.17	0.45	0.46	0.03
LOI	3.72	15.23	39.19	44.43	24.88	28.93	25.11	1.31
sum	100.07	100.23	99.92	99.22	99.63	99.36	99.72	99.92

	Coconino							impact-melt
	C-3†	MC-02	MC-04	MC-05	MC-05	MC-09	MC-11a	H11‡
SiO_2	71.83	97.81	95.48	96.30	96.12	92.15	99.12	48.27
TiO_2	0.02	0.04	0.09	0.06	0.07	0.14	0.02	0.20
Al_2O_3	0.96	1.14	2.63	2.17	2.26	4.11	0.72	2.90
Fe_2O_3	0.02	0.05	0.20	0.29	0.08	0.13	0.14	7.05
FeO	0.05	0.06	0.11	0.05	0.06	0.06	0.06	16.48
MnO	0.00	0.00	0.00	0.00	0.00	0.00	0.00	0.08
MgO	0.78	0.00	0.04	0.05	0.06	0.22	0.00	8.24
CaO	14.55	0.10	0.13	0.10	0.11	0.45	0.05	12.00
Na_2O	0.00	0.00	0.00	0.00	0.01	0.00	0.00	0.09
K_2O	0.13	0.18	0.52	0.59	0.60	0.60	0.07	0.32
P_2O_5	0.13	0.02	0.03	0.03	0.03	0.04	0.02	0.44
LOI	12.01	0.53	0.96	0.75	0.75	1.77	0.37	1.40
sum	100.48	99.93	100.19	100.39	100.15	99.67	100.57	97.47

†This sample from an undocumented location is anomalous in CaO content, likely reflecting secondary calcite cement.
‡H11 is a composite of 15 impact-melt particles. See Appendix 3.

TABLE 2. COMPOSITIONS OF METEOR CRATER TARGET ROCKS DETERMINED BY INSTRUMENTAL NEUTRON ACTIVATION ANALYSIS

		Moenkopi Formation							Kaibab Formation																
		Ma	Mb	Mc	Md	Me	MC-01	MC-07	Ka	Kb	Kc	Kd	Ke	Kf	Kg	Kh	Ki	Kj	Kk	Kl	MC-06	MC-10	MC-12	K-1	K-2
mass†	mg	105.33	81.18	70.64	72.05	84.83	62.99	73.91	109.88	98.15	94.31	102.02	80.19	87.40	81.43	93.46	91.30	92.20	101.52	87.05	66.05	79.30	63.85	72.87	66.84
Na	µg/g	284	358	363	355	372	322	349	229	364	300	272	295	263	270	259	236	222	249	213	478	269	246	389	222
K_2O	wt%	1.16	1.46	1.69	1.53	1.44	1.22	1.24	0.48	0.46	0.72	0.53	0.56	0.58	0.260	0.61	0.269	0.50	0.58	0.70	0.45	0.49	*0.234*	0.222	0.043
CaO	wt%	7.2	9.3	8.4	10.6	13.1	2.0	15.0	13.5	18.0	11.7	17.4	17.2	17.4	24.6	15.7	24.6	18.0	18.6	15.4	15.2	19.2	16.0	26	29
Sc	µg/g	3.98	6.54	8.02	7.29	6.51	3.84	4.87	0.96	0.91	1.17	1.07	1.01	1.23	0.604	1.63	0.89	0.772	1.41	2.38	0.722	1.08	0.96	0.625	0.159
Cr	µg/g	24.0	29.3	32.4	24.1	27.3	15.7	37.2	30.6	23.9	32.9	32.3	27.3	28.6	8.2	15.6	8.0	22.6	14.4	23.8	28.0	25.4	34.8	12.2	5.6
Fe	mg/g	6.49	15.46	19.10	20.25	17.26	8.21	13.20	2.13	2.18	1.53	3.11	2.09	2.68	2.14	2.67	3.45	3.49	4.14	11.70	1.68	2.04	4.80	1.29	3.72
Co	µg/g	7.48	5.13	5.81	10.5	8.8	2.47	4.32	3.08	2.86	1.65	1.99	1.55	1.60	0.83	0.96	1.01	1.08	2.09	15.0	1.70	1.82	2.86	1.49	2.14
Ni	µg/g					14	16		7	8	8	11	13	10	7	7	6	5	9	37	8	10	20	10	10
Zn	µg/g	33	44	58	82	59	22.2	36	19.6	21.6	18.5	19.1	16.1	18.2	24.0	24.5	27.9	22.1	26.8	64	27.8	13.0	132		
As	µg/g	7.3	3.30	4.14	6.2	4.21	1.55	3.12	1.48	1.27	1.44	6.38	2.40	1.61	2.14	4.71	1.65	3.13	9.8	22.0	9.4	*1.00*	11.4	2.16	1.91
Se	µg/g		0.4						1.2	1.4	1.1	0.88	1.3	0.9	0.10	0.22			0.14		1.0	1.49	1.3		
Br	µg/g	0.42	0.46	0.45	0.43	0.53	*0.18*	0.40	1.10	1.26	1.00	2.0	1.46	1.02	2.2	1.28	1.10	1.07	0.81	0.79	1.36	1.07	1.00	3.0	1.07
Rb	µg/g	33	48	56	46	46	38	40	13.3	12.0	19.0	14.4	14.8	16.0	7.2	16.7	8.2	14.0	16.8	20.9	12.9	13.9	6.6	*6.1*	
Sr	µg/g	74	80	82	73	93	72	88	310	89	75	108	101	149	87	107	97	109	102	101	67	97	70	110	87
Zr	µg/g	460	360	230	150	210	370	470	140	100	200	140	160	150	58	160	61	150	90	200	140	100	100	55	
Sb	ng/g	374	451	530	440	440	343	389	203	160	199	285	176	177	131	197	104	166	218	500	287	140	560	118	*40*
Cs	µg/g	1.82	5.22	5.96	3.37	4.34	1.97	3.59	0.64	0.65	0.89	0.89	0.66	0.89	0.319	0.75	0.434	0.71	1.20	1.36	0.61	0.84	0.419	0.330	*0.052*
Ba	µg/g	207	440	308	304	269	191	207	198	88	229	180	137	151	64	193	78	114	105	140	142	97	63	65	*16*
La	µg/g	9.8	16.4	17.8	14.4	16.7	11.2	19.5	4.82	3.60	4.84	4.19	4.04	6.57	2.26	4.18	2.68	5.07	5.00	7.78	4.02	4.45	8.8	2.13	0.736
Ce	µg/g	21.0	33.1	36.1	29.5	33.0	25.0	38.0	8.4	6.5	8.7	7.4	7.3	8.5	4.06	7.4	4.56	8.0	8.4	14.1	7.6	7.9	7.2	4.20	*1.33*
Nd	µg/g	11	14	17	13	16	13	21	5.1	3.0	4.9	3.7	3.7	5.1	2.2	4.2	2.9	5.2	4.7	8.4	4.1	4.6	7	*1.8*	
Sm	µg/g	2.65	3.65	3.84	3.45	3.74	2.79	4.32	1.24	0.74	0.96	0.87	0.83	1.11	0.463	0.89	0.541	0.93	0.89	1.65	0.69	0.87	1.40	0.426	0.155
Eu	µg/g	0.65	0.84	0.88	0.81	0.86	0.69	0.92	0.289	0.159	0.211	0.191	0.181	0.233	0.091	0.203	0.110	0.191	0.182	0.365	0.148	0.197	0.286	0.089	*0.029*
Tb	µg/g	0.415	0.56	0.56	0.52	0.55	0.411	0.66	0.173	0.099	0.129	0.126	0.111	0.160	0.060	0.126	0.074	0.124	0.116	0.240	0.086	0.120	0.198	0.057	*0.026*
Yb	µg/g	1.82	2.17	1.91	1.68	1.98	1.51	2.65	0.55	0.432	0.61	0.57	0.55	0.73	0.271	0.57	0.345	0.55	0.52	0.94	0.446	0.52	0.87	0.256	*0.083*
Lu	µg/g	0.292	0.336	0.294	0.253	0.303	0.235	0.420	0.090	0.071	0.103	0.096	0.090	0.118	0.040	0.090	0.055	0.088	0.081	0.146	0.077	0.085	0.130	0.043	0.027
Hf	µg/g	13.0	10.2	6.2	4.64	6.1	11.1	16.0	4.18	2.87	5.6	4.11	4.46	4.12	1.53	4.14	1.63	3.88	2.55	5.39	4.68	3.11	2.99	1.71	0.36
Ta	ng/g	580	540	500	390	500	570	690	197	144	211	167	151	163	81	137	86	138	144	254	177	167	108	68	9
W	ng/g	770	800	820	650	710	630	850	270	200	270	210	200	200	200	230	160	240	280	460	400	180	310	210	*80*
Au	ng/g			*0.6*					1.1	*0.4*	*0.6*	2.8	*0.4*	*0.5*	1.2	*0.5*	1.0	2.0	2.3		0.7	*0.6*	20.2	1.4	0.7
Th	µg/g	3.69	4.87	5.26	4.25	4.54	3.44	5.97	1.09	0.91	1.27	1.03	1.00	1.19	0.461	0.94	0.58	1.02	1.12	1.80	0.90	0.96	0.92	0.55	*0.090*
U	µg/g	1.73	1.55	1.60	1.83	1.56	1.16	2.25	3.06	2.40	2.85	2.41	2.76	2.08	2.20	1.40	1.70	1.41	1.20	1.53	3.37	2.04	4.7	1.34	1.86

(continued)

TABLE 2. COMPOSITIONS OF METEOR CRATER TARGET ROCKS DETERMINED BY INSTRUMENTAL NEUTRON ACTIVATION ANALYSIS *(continued)*

		Toroweap Formation				Coconino Formation														
		Ta	Tb	MC-08	MC-13	Ca	Cb	Cc	Cd	MC-02	MC-03	MC-04	MC-05	MC-09	MC-11a	MC-11b	C-1	C-2	C-3‡	C-4
mass†	mg	105.98	97.53	77.33	65.78	117.32	108.48	133.77	117.47	71.98	64.39	76.93	76.07	65.33	65.16	72.15	116.90	127.84	80.82	85.3
Na	µg/g	74.1	119	49.6	154	132	90.2	55.9	60.5	39.1	62.5	31.2	37.5	126	*22.9*	*16.4*	128	73	88	27.3
K_2O	wt%	0.284	0.43	0.192	0.66	0.216	0.238	0.158	0.184	0.137	0.236	0.115	0.146	0.46	*0.085*	*0.038*	0.35	0.28	0.135	0.106
CaO	wt%	0.15	1.53	*0.30*	3.4	0.07	0.09	0.06	*0.13*					0.26					13.7	0.05
Sc	µg/g	0.514	1.18	0.393	0.775	0.714	1.05	0.490	0.479	0.496	1.03	0.479	0.353	1.27	0.421	0.222	1.25	0.639	0.369	0.342
Cr	µg/g	17.6	18.5	12.6	36.4	9.4	18.2	11.0	12.7	4.3	7.6	4.0	7.9	14.3	*2.6*	*1.7*	11.9	7.6	9.2	*3.0*
Fe	mg/g	0.892	1.017	0.378	0.696	0.530	0.570	0.363	0.438	0.338	0.527	0.357	0.284	0.830	1.524	0.469	0.581	0.427	0.277	0.257
Co	µg/g	0.83	0.70	0.187	0.427	1.25	0.426	0.239	0.203	0.166	0.265	0.104	0.118	0.61	0.328	0.311	4.31	0.389	0.64	0.157
Ni	µg/g	4							2										9	
Zn	µg/g	7.3	9.9	2.5	5.5	7.2	5.7	2.9	3.6	3.4	4.5	2.2	2.2	10.4	12.3	5.1				
As	µg/g	5.84	2.55	*0.59*	1.65	0.69	1.12	0.42	1.17	0.57	1.51	0.78	0.79	2.01	5.7	2.11	1.42	0.77	1.06	0.49
Se	µg/g		0.14												0.95	0.44			0.15	
Br	µg/g	0.40	0.46	0.36	0.62	0.32	0.38	0.29	0.35	0.23	0.20	0.22	0.27	0.38	0.28	0.28	0.44	0.31	1.91	0.34
Rb	µg/g	8.0	11.8	5.2	19.3	6.2	7.0	4.5	5.3	4.0	7.0	3.9	3.6	12.9	2.5	*1.3*	10.1	7.7	3.4	3.4
Sr	µg/g	137	188	*8*	600	29	38	28	38	25	33	16	36	48	11	*8*	43	23	90	23
Zr	µg/g	73	130	150	150	110	120	43	70	40	120	48	32	120	21	21	100	16	28	17
Sb	ng/g	186	170	155	196	72	99	76	102	67	95	64	74	1000	104	63	119	82	68	64
Cs	µg/g	0.417	0.57	0.276	1.02	0.270	0.399	0.268	0.283	0.295	0.468	0.263	0.245	0.69	0.233	0.138	0.51	0.38	0.217	0.197
Ba	µg/g	49	312	154	186	374	151	215	163	88	154	272	101	510	8	7	520	184	240	*17*
La	µg/g	3.62	4.22	1.04	13.8	3.63	5.15	2.94	2.94	3.31	5.46	2.46	2.60	5.36	2.74	2.06	6.24	3.27	2.40	2.14
Ce	µg/g	6.8	8.2	1.97	28.1	6.70	9.4	4.98	5.09	6.1	10.7	3.98	4.47	10.2	5.37	4.29	12.6	6.1	4.06	3.46
Nd	µg/g	2.8	4.5	*1.2*	17	3.5	4.6	2.9	3.1	3.0	4.5	*1.7*	3.2	5.1	2.8	*2.0*	7	3.3	3.6	*1.3*
Sm	µg/g	0.619	0.79	0.233	2.82	0.71	0.96	0.560	0.550	0.607	0.94	0.424	0.445	1.10	0.506	0.354	1.17	0.627	0.530	0.456
Eu	µg/g	0.136	0.189	0.058	0.614	0.149	0.203	0.117	0.103	0.124	0.192	0.089	0.081	0.246	0.112	0.075	0.246	0.139	0.103	0.102
Tb	µg/g	0.082	0.115	0.075	0.257	0.088	0.145	0.066	0.059	0.076	0.119	0.061	0.047	0.137	0.064	0.045	0.133	0.072	*0.064*	0.069
Yb	µg/g	0.305	0.403	0.55	0.61	0.412	0.66	0.232	0.243	0.277	0.53	0.246	0.169	0.55	*0.186*	*0.159*	0.64	0.246	*0.217*	0.258
Lu	µg/g	0.047	0.066	0.087	0.095	0.065	0.102	0.0363	0.039	0.040	0.082	0.034	0.0251	0.089	0.028	0.022	0.106	0.038	0.037	0.038
Hf	µg/g	1.99	3.41	4.45	4.70	2.91	3.39	1.18	1.90	1.31	3.61	1.34	0.87	3.77	0.70	0.58	4.18	0.76	1.43	0.64
Ta	ng/g	81	101	62	222	79	154	49	59	53	149	49	36	163	42	*23*	179	57	*44*	29
W	ng/g	220	240	140	510	200	280	110	130	100	220	110	60	300	*80*	*60*	300	*80*	*140*	60
Au	ng/g	1.6	1.6	*0.7*	*1.2*	1.9	1.8	0.36	0.9	1.8		*0.5*	*0.3*	*1.4*			1.8	2.1	2.3	0.44
Th	µg/g	0.86	0.87	0.56	2.25	0.83	1.21	0.63	0.67	0.73	1.22	0.63	0.50	1.32	0.60	0.42	1.47	0.76	0.60	0.47
U	µg/g	1.40	1.50	0.89	1.73	0.50	0.91	0.44	0.75	0.38	0.69	0.46	0.48	0.90	*0.24*	*0.15*	0.81	0.38	1.14	0.36

Note: In this table, Ni is given in units of µg/g. Ir in all target rocks was below the 2σ detection limit of ~1 ng/g. Typical 1σ relative uncertainties are: ≤2%—Na, Sc, Fe, Co, La, Sm; 1–3%—Cr, As, Cs, Ce, Eu, Yb, Hf, Th, U; 2–5%—K_2O, CaO, Zn, Sb, Ba, Tb, Lu, Ta; 4–8%—Br, Rb; 5–10%—Se; 5–20%—Sr, Au; 10–20%—Zr, Nd W; 15–50%—Ni. Values in italics have uncertainties 1.33–3× the upper end of the typical uncertainty range. Underlined values have uncertainties 3–6× the upper end of the typical uncertainty range. In all cases, the proper number of significant digits is used.

†Mass refers to weight in mg of analyzed material; samples were splits of homogenized powders of much larger mass.

‡This sample from an undocumented location is anomalous in CaO content, likely reflecting secondary calcite cement. The CaO content of most Coconino samples was below the instrumental neutron activation analysis detection limit.

TABLE 3. COMPOSITIONS OF METEOR CRATER IMPACT-MELT PARTICLES DETERMINED BY INSTRUMENTAL NEUTRON ACTIVATION ANALYSIS

samples‡		IIG-1a	IIG-1b	IIG-2a	IIG-2b	IIG-3a	IIG-3b	IIG-3c	IIG-3d	IIG-4	SIG-1	SIG-2	SIG-3	SIG-4	M1	M3a	M3b	M4a	M5	M6	M7	M8a	M8b
mass†	mg	83.16	107.47	78.63	98.38	100.52	87.19	20.05	31.29	25.5	9.43	79.08	0.84	27.05	50.34	52.81	50.47	50.93	38.54	48.57	48.94	49.70	63.17
Na	µg/g	433	421	608	496	507	415	464	558	130	240	125	209	179	214	157	150	151	171	284	157	206	384
K_2O	wt%	0.35	0.32	0.38	0.31	0.34	0.32	0.289	0.381	0.134	0.218	0.099	*0.17*	0.353	0.202	0.216	0.201	0.134	0.140	0.26	*0.097*	0.40	0.50
CaO	wt%	*12.1*	*12*	*7.3*	*8*	*10*	9.7	10.4	10.1	16.0	*14*	*13*	13	13.4	14.8	10.0	10.0	14.3	12.8	10.9	13.6	9.1	8.4
Sc	µg/g	2.00	1.98	2.38	2.17	2.19	1.96	2.30	2.47	2.36	1.99	1.89	1.86	1.37	1.50	1.59	1.55	1.74	1.90	2.22	1.69	2.36	2.90
Cr	µg/g	84	84	80	81	83	85	80	80	86	80	91	*91*	84	82	82	84	78	81	79	86	73	72
Fe	mg/g	180	184	178	190	180	184	183	179	210	183	245	202	206	196.2	210.6	215.7	171.5	201.7	163.3	220.5	149.3	135.5
Co	µg/g	910	880	824	910	826	870	828	772	940	870	1030	930	1010	912	960	1000	782	776	722	1020	687	589
Ni	mg/g	14.0	12.6	12.5	14.0	11.5	12.4	11.5	10.4	15.3	14.2	17.7	15.9	16.3	13.7	13.6	14.2	11.9	12.3	9.6	15.9	9.5	8.1
Zn	µg/g														32			28	34	35	33		62
As	µg/g	7.2	6.3	7.1	6.7	6.1	6.0	7.7	6.4	2.58	2.9	13.4	3.6	7.3	5.1	14.3	14.1	2.49	7.6	11.6	2.4	6.6	6.6
Se	µg/g	1.0	0.7		0.8	0.8	0.7	0.7														0.6	
Br	µg/g	0.37	0.31	0.39	*0.32*	0.35	0.35	0.70	0.43	0.45	1.0	0.26	6.8	0.48	0.76	0.74	0.81	0.30	1.0	1.9	*0.21*	0.59	0.65
Rb	µg/g			14	17	16	11	14															20
Sr	µg/g																						
Zr	µg/g	130	150	180	110	160	150	180	240	220	230	180		160	150	150	120	140	210	250	190	170	160
Sb	ng/g	260	230	300	260	230	220	280	260	160	*170*	170		210	170	220	220	110	260	270	120	320	380
Cs	µg/g	0.82	0.81	1.05	0.98	0.91	0.81	0.68	1.05	0.27	0.7			0.74	0.42	0.44	0.41	0.26	0.30	0.62	0.26	1.18	1.53
Ba	µg/g	430	470	540	550	470	500	530	610	300	*190*	270		1960	530	820	810	240	690	410	180	320	300
La	µg/g	13.2	13.9	16.6	17.4	11.6	10.0	19.5	16.6	18.0	9.3	11.7	7.0	5.81	4.90	8.6	8.3	9.0	10.2	13.3	22.2	11.0	15.0
Ce	µg/g	25.7	28.3	34.2	37.7	20.6	17.8	33.6	29.4	42.2	17.1	23.3	21	9.2	9.5	13.3	12.9	14.6	14.2	18.7	23.5	16.9	23.0
Nd	µg/g	*15*	16	21	15	14	14	15	13	16		11			6			11	12	13	24	17	16
Sm	µg/g	2.39	2.50	3.01	3.11	2.06	1.83	3.39	2.98	3.49	1.90	2.33	1.56	1.11	1.06	1.60	1.54	1.80	1.98	2.34	3.75	1.95	2.66
Eu	µg/g	0.57	0.58	0.71	0.73	0.48	0.43	0.78	0.70	0.80	*0.41*	0.57	0.32	*0.23*	0.252	0.38	0.37	0.43	0.47	0.57	0.92	0.46	0.62
Tb	µg/g	0.36	0.41	0.49	0.42	0.32	0.26	0.45	0.39	0.43	*0.35*	0.41		*0.18*	0.15	0.26	0.21	0.26	0.28	0.33	0.53	0.25	0.36
Yb	µg/g	1.04	1.10	1.32	1.27	1.00	0.91	1.44	1.29	1.43	0.97	1.05	0.8	0.68	0.64	0.84	0.75	0.88	1.00	1.16	1.42	0.83	1.06
Lu	µg/g	0.161	0.165	0.197	0.186	0.144	0.138	0.22	0.196	0.201	*0.14*	0.149	0.12	*0.12*	0.091	0.126	0.116	0.125	0.133	0.172	0.194	0.134	0.153
Hf	µg/g	3.86	4.03	4.17	3.72	3.80	3.87	4.5	4.3	5.0	4.6	4.4	3.4	4.7	4.5	4.5	4.2	4.6	5.2	5.9	4.4	4.43	4.9
Ta	ng/g	250	250	250	280	270	240	230	250	360	400	260		230	240	240	220	270	270	270	220	260	280
W	ng/g	400	300	400		350	360	300	200			270		320	280		350			270		290	
Ir	ng/g	450	410	360	410	370	390	410	360	285	360	460	*350*	580	460	530	560	382	448	388	374	359	302
Au	ng/g	160	142	124	150	101	113	87	117	*11*	62	24	37	314	110	251	256	28.7	101	71	50	124	115
Th	µg/g	2.1	2.1	2.4	2.4	2.0	1.81	2.4	2.3	3.3	1.6	2.1	*2.5*	*1.4*	1.43	1.66	1.7	1.7	1.78	2.0	1.6	2.06	2.59
U	µg/g	1.20	1.03	0.86	0.70	0.95	1.69	0.83	0.91	*0.23*	0.87	0.43		1.69	1.10	2.33	2.29	0.39	0.74	0.66	0.71	0.93	1.11

(continued)

TABLE 3. COMPOSITIONS OF METEOR CRATER IMPACT-MELT PARTICLES DETERMINED BY INSTRUMENTAL NEUTRON ACTIVATION ANALYSIS *(continued)*

		M10	M11	M12	M13a	M13b	M14	M15	M16	M17	M18a	M18b	M19	M20	M21	M22	M23	M24	M25	M26	M27	H11	H11a
mass†	mg	50.33	50.56	44.06	49.01	44.40	47.86	37.00	57.45	29.48	48.89	28.67	25.59	5.10	32.17	35.20	30.47	33.75	32.93	9.54	22.52	78.25	67.24
Na	µg/g	232	411	425	356	204	114	263	166	264	753	841	384	1870	234	153	200	176	125	167	570	299	208
K_2O	wt%	0.32	0.45	1.23	0.26	0.160	0.167	0.52	0.31	0.256	0.49	0.28	0.41	*0.49*	0.169	0.154	0.158	0.222	0.079	0.127	0.30	0.32	0.33
CaO	wt%	12.9	16.0	14.6	8.4	11.1	9.0	18.6	11.1	12.0	18.0	18.4	13.3	2.8	17.7	12.2	18.2	*10.8*	13.4	15.2	16.1	11.2	12.9
Sc	µg/g	1.67	2.17	4.20	2.87	1.84	1.46	1.64	1.83	1.54	1.63	1.75	1.32	3.81	2.19	3.50	2.07	1.82	1.66	1.74	1.86	2.26	1.84
Cr	µg/g	80	58	34.4	87	87	86	58	76	74	51.5	54	58	69	66	86	66	86	89	74	67	78	75
Fe	mg/g	191.3	71.0	42.9	187.4	186.9	181.4	79.5	141.7	151.4	55.2	58.0	97.7	67.0	100.3	235.0	104.5	192.8	218.9	177.0	129.0	173.1	159.9
Co	µg/g	891	311	169	700	785	792	372	584	694	244	248	452	285	417	757	435	903	1020	733	518	763	744
Ni	mg/g	11.3	4.71	2.48	9.0	9.1	11.0	5.8	7.1	9.2	3.87	3.88	6.1	*1.48*	7.2	13.2	7.4	13.1	15.9	12.0	8.5	10.0	9.4
Zn	µg/g		*25*	*16*				15	33		13	18		77	25	21					21	29	101
As	µg/g	5.3	5.4	*0.28*	28.9	11.7	14.1	1.52	8.0	19.4	2.95	3.36	7.0	13.4	6.5	30.2	5.70	12.4	4.4	6.2	5.4	7.6	5.2
Se	µg/g	1.2					0.9						0.7										0.6
Br	µg/g	0.8	2.4	*0.10*	4.4	3.4	1.7	1.23	3.2	2.2	1.24	2.0	1.40	5.0	0.60	0.53	0.40	0.65	0.36	0.73	0.32	1.1	0.57
Rb	µg/g	16	15	39				18	11		17	10	16								8		
Sr	µg/g										580	640		350									
Zr	µg/g	160	230	320	190	190	110	200	260	200	240	220	190	500	160	310	180	190	160	210	230	150	160
Sb	ng/g	190	310	150	440	220	220	150	370	160	160	90	160	*130*	140	260	100	310	*80*	*130*	170	260	200
Cs	µg/g	0.63	1.01	3.23	0.53	0.27	0.52	0.92	0.52	0.44	0.85	0.50	0.67	0.56	0.44	0.24	0.29	0.49	0.21	0.25	0.52	0.78	0.65
Ba	µg/g	930	470	273	600	430	270	580	420	4900	10100	13400	6400	2110	200	390	220	470	160	320	690	540	670
La	µg/g	8.0	7.87	14.6	23.1	10.6	5.23	7.83	13.2	4.69	6.75	5.44	4.83	9.0	9.1	24.6	6.05	10.6	6.62	8.3	7.83	12.2	7.86
Ce	µg/g	13.9	14.6	28.1	27.8	14.0	9.8	12.3	18.3	9.3	11.6	11.1	9.0	25.9	19.5	47.3	18.8	19.1	10.8	13.0	13.7	22.4	14.3
Nd	µg/g	11	7	13	24	13		7	14	8	6	7			11	29	6	10	5		6	13	
Sm	µg/g	1.48	1.50	2.98	4.63	1.97	1.06	1.47	2.47	1.04	1.33	1.23	0.98	1.92	2.08	6.23	1.46	1.98	1.43	1.72	1.64	2.33	1.54
Eu	µg/g	0.34	0.341	0.65	1.11	0.47	0.246	0.322	0.59	0.239	0.304	0.288	0.226	0.43	0.50	1.51	0.350	0.47	0.36	0.41	0.37	0.54	0.354
Tb	µg/g	0.20	0.215	0.419	0.65	0.29	0.15	0.202	0.36	0.15	0.203	0.185	0.14	0.32	0.30	0.93	0.22	0.27	0.21	0.24	0.24	0.34	0.22
Yb	µg/g	0.83	0.86	1.62	1.85	1.02	0.65	0.88	1.15	0.65	0.82	0.76	0.66	1.18	0.95	2.30	0.85	0.94	0.72	1.03	0.90	1.095	0.94
Lu	µg/g	0.135	0.138	0.248	0.258	0.145	0.096	0.146	0.167	0.107	0.122	0.114	0.103	0.17	0.146	0.334	0.126	0.139	0.102	0.146	0.139	0.163	0.141
Hf	µg/g	5.2	5.9	8.3	5.9	4.9	4.4	5.3	6.6	4.98	6.1	6.2	5.3	13.4	5.2	6.6	5.6	4.7	3.92	4.8	5.5	5.1	5.1
Ta	ng/g	220	270	520	260	200	220	240	260	210	270	290	220	570	310	340	290	240	200	*210*	240	240	230
W	ng/g	600	400	570	410	220	200	290	200	400	380	260	320	400	190	440	190						500
Ir	ng/g	479	169	2.4	421	405	437	133	321	433	93	101	255	91	160	400	183	518	485	403	259	380	350
Au	ng/g	164	85	2.3	157	139	202	21.7	112	180	19.8	15.1	122		*7.0*	24.5	*4.0*	243	57	40	25.9	124	93
Th	µg/g	1.6	1.93	4.05	3.3	1.74	1.35	1.66	1.8	1.44	1.70	1.76	1.35	3.9	2.12	5.3	2.03	1.81	1.36	1.62	1.75	2.31	1.8
U	µg/g	1.6	1.57	1.91	0.55	0.53	1.13	2.08	0.33	1.52	1.98	1.31	1.85	0.88	0.32	0.66	0.32	0.78	0.26	0.77	0.89	1.28	1.65

Note: In this table, Ni is given in units of mg/g. Typical 1σ relative uncertainties are: ≤2%—Na, Sc, Fe, Co, Ni, La, Sm; 1–3%—Cr; 1–4%—As, Ce, Eu, Hf, Ir; 1–5%—Yb, Au; 2–6%—K_2O, CaO, Lu; 2–8%—Ba, Th; 2–12%—Tb, U; 2–16%—Cs; 4–5%—Sr; 4–12%—Sb; 5–20%—Zn, Br, Ta; 10–35%—Zr; 10–50%—Rb, Nd, W; 25–45%—Se. Values in italics have uncertainties 1.33–3× the upper end of the typical uncertainty range. Underlined values have uncertainties 3–6× the upper end of the typical uncertainty range. In all cases, the proper numbers of significant digits are used.

†Mass refers to weight in mg of analyzed material and represents most or all of the mass of sample prepared. H11 is an exception; this is a split of homogenized powder prepared by combining 15 impact-melt particles.

‡Samples IIG-1a, IIG-1b, etc., and M3a, M3b are different splits of individual impact-melt particles run as homogeneity tests. Sample M8a is hand-picked fresh interior glass, while M8b is fine dust produced during crushing of an individual impact-melt particle. Samples M13a and M13b are exterior and interior sample pairs, respectively, from an individual impact-melt particle. Samples M18a and M18b are interior and exterior sample pairs, respectively, from an individual impact-melt particle. H11a is an individual impact-melt particle from the same group as used for sample H11.

TABLE 4. MAJOR-ELEMENT COMPOSITIONS OF IMPACT-MELT PARTICLES DETERMINED BY ELECTRON MICROPROBE ANALYSIS OF FUSED BEADS

	IIG-1a	IIG-2a	IIG-3a	IIG-4	M1	M3	M4	M7	M8	M10
SiO_2	47.9	51.8	50.9	41.7	43.0	47.7	43.4	45.3	54.4	47.6
TiO_2	0.19	0.20	0.18	0.22	0.17	0.19	0.18	0.19	0.20	0.23
Al_2O_3	3.10	3.47	3.30	3.41	2.54	3.04	2.74	2.92	3.88	3.23
Cr_2O_3	0.01	0.02	0.01	0.01	0.01	0.02	0.02	0.02	0.01	0.01
FeO	25.3	27.4	25.5	22.7	26.3	28.4	24.7	27.7	20.9	25.2
MnO	0.12	0.17	0.10	0.12	0.03	0.07	0.05	0.05	0.06	0.06
MgO	8.67	5.93	7.83	12.0	10.7	9.44	10.9	9.06	8.6	8.70
CaO	13.6	9.38	11.0	19.2	16.6	10.4	17.4	13.8	11.1	14.0
Na_2O	0.07	0.08	0.07	0.02	0.03	0.03	0.03	0.05	0.03	0.05
K_2O	0.39	0.42	0.37	0.19	0.19	0.27	0.15	0.21	0.42	0.42
P_2O_5	0.74	1.14	0.63	0.47	0.35	0.43	0.44	0.77	0.37	0.46

	M11	M13	M14	M15	M16	M17	M18	M19	SIG-4
SiO_2	55.6	50.0	51.9	52.0	51.9	52.1	54.5	57.9	44.6
TiO_2	0.24	0.22	0.16	0.20	0.26	0.18	0.21	0.16	0.18
Al_2O_3	3.40	3.19	2.70	2.95	3.24	2.79	3.25	2.68	2.86
Cr_2O_3	0.01	0.02	0.02	0.01	0.05	0.01	0.01	0.01	0.02
FeO	9.05	26.0	24.9	11.3	20.3	20.7	7.93	12.7	30.3
MnO	0.07	0.09	0.05	0.08	0.11	0.03	0.04	0.03	0.07
MgO	12.4	8.78	9.09	13.2	10.6	10.2	13.8	11.1	8.47
CaO	18.5	11.0	10.7	19.4	12.8	13.3	19.5	14.7	12.5
Na_2O	0.06	0.06	0.03	0.04	0.03	0.04	0.12	0.06	0.03
K_2O	0.43	0.29	0.21	0.32	0.38	0.26	0.39	0.37	0.38
P_2O_5	0.25	0.38	0.30	0.48	0.30	0.33	0.33	0.31	0.58

TABLE 5. COMPOSITIONS OF METALLIC SPHERULES AND THE REMBANG IVA IRON DETERMINED BY INSTRUMENTAL NEUTRON ACTIVATION ANALYSIS*

Spherule #:		1	2	3	4	5	6	7	8	9	10	11	12	14
mass	(mg):	9.03	12.58	8.53	9.35	11.24	3.32	12.83	8.60	9.40	5.08	3.96	4.36	2.12
Fe	mg/g:	818	716	815	714	800	570	768	740	772	834	759	637	614
Co	mg/g:	7.6	9.3	8.9	5.6	9.1	7.5	10.4	11.1	10.0	7.3	10.7	3.1	3.2
Ni	mg/g:	128	152	152	86.6	148	124	169	181	166	115	171	50.2	38.9
Ga	µg/g:	92.3†	88.2†	120	83.5†	110	170	81.8†	–	50	–	–	80	90
Ge	µg/g:	514†	772†	–	485†	–	–	795†	–	–	–	–	–	–
As	µg/g:	44.1	49.5	48.0	24.0	48.2	66.8	51.9	63.8	52.1	25.8	64.9	19.0	27.5
Ir	µg/g:	4.48	5.53	5.4	3.14	4.9	9.15	6.07	6.62	5.83	4.18	6.75	2.61	1.96
Au	µg/g:	3.17	3.85	3.86	2.11	3.74	1.99	4.3	4.57	4.26	2.72	4.69	1.28	0.63
Σ(Fe, Co, Ni) :		954	877	976	806	957	702	947	932	948	956	941	690	656

Spherule # :		15	16	17	18	19	20	21	23	Rembang‡			
										this work	WR01	WR01	S96
mass	(mg):	5.21	5.24	0.72	3.25	9.39	3.80	2.21	2.38	16.7			
Fe	mg/g:	820	748	676	783	726	745	653	788	943	–	–	–
Co	mg/g:	8.0	11.3	3.3	9.7	12.6	9.6	2.8	7.7	4.0	4.03	4.03	4
Ni	mg/g:	130	182	41.1	155	216	164	31.3	137	89.6	85.4	88.4	–
Ga	µg/g:	–	–	–	–	–	–	–	–	–	–	–	–
Ge	µg/g:	–	–	–	–	–	–	–	–	–	–	–	–
As	µg/g:	41.7	94.9	20.7	47.9	84.8	44.4	13.7	43.0	9.4	8.85	8.93	9
Ir	µg/g:	4.73	6.77	2.24	5.69	7.57	5.76	1.59	5.09	1.19	1.16	1.16	1.14
Au	µg/g:	3.51	4.57	0.75	4.11	5.59	4.09	0.55	3.58	1.19	1.78	1.75	1.91
Σ(Fe, Co, Ni):		958	941	720	948	955	919	687	933	1037			

*Typical instrumental neutron activation analysis 1σ relative uncertainties are: 1%—Fe, Co; 2%—Au; 1–3%—Ni; 2–4%—Ir; 5–10%—As; 30–50%—Ga.

†These analyses done by radiochemical neutron activation analysis, typical 1σ relative uncertainties are 4%.

‡WR01 – Wasson and Richardson (2001); S96—Scott et al. (1996).

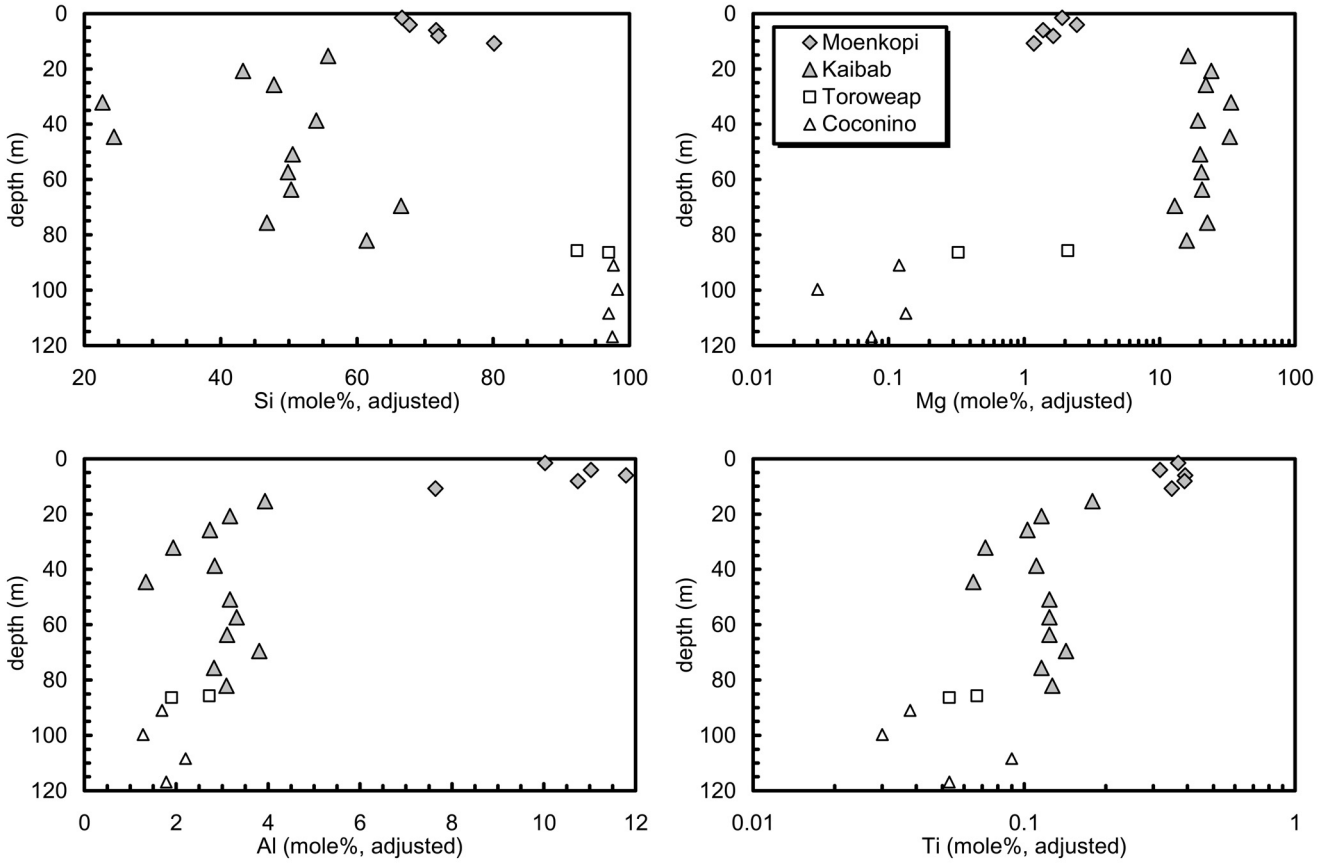

Figure 1. Variation in major-element compositions of Meteor Crater target rocks with depth demonstrating the geochemical characteristics of the different formations. On all figures, lithophile element data are adjusted to a volatile- and Fe-free basis to correct for differences in CO_2 and H_2O in the target rocks, and differences in projectile components in impact-melt particles. See text for a discussion of this. Note that Mg and Ti are plotted on log scales. Data from See et al. (2002).

However, the scatter in the data would *permit* a small Toroweap or Coconino component. The expansion of the impact-melt field in the Mg-Al plot demonstrates that the data distribution could obscure at most ~10% Coconino contribution. Because there are no distinguishing elements in the Toroweap or Coconino, they are difficult to fingerprint in impact melts.

Lithophile-trace-element contents of impact-melt particles and target rocks are in accord with the above inference. In Ca-Sc and Ca-Ta plots, the impact-melt particles plot between the fields occupied by Kaibab and Moenkopi rocks and away from the trace-element-poor Toroweap and Coconino (Fig. 4). The Toroweap and Coconino rocks have the lowest lithophile-trace-element contents (Table 2, Fig. 2), and these elements are generally correlated in the target rocks. Thus, on diagrams such as Ta versus Sc (Fig. 4), Toroweap and Coconino rocks could be interpreted as one end member of a mixing trend. However, their stratigraphic location argues against this. The Ta-Sc plot clearly shows that the topmost unit, the Moenkopi, is a significant component of the impact-melts, and that all of them lie between the fields for Moenkopi and Kaibab rocks. Because the Kaibab is a thick unit between the Moenkopi and Toroweap/Coconino, it is more plausible that the Kaibab is the most significant trace-element-poor component in the impact-melts.

The impact-melt particles exhibit substantial heterogeneity in lithophile element contents (Figs. 3 and 4). Some particles fall within the field of Kaibab rocks in major element composition (Fig. 3) and could contain only this target component. None fall within the field of Moenkopi rocks for major elements (Fig. 3), although some do so for trace elements (Fig. 4). (We have trace element data for a larger suite of samples than we do for major elements.) The Moenkopi and Kaibab rocks each show substantial ranges in composition, thus impact-melt particles that plot within the fields for either of the target rocks are not necessarily composed of only that target component. Note that all of the impact-melt particles (this work) and pure glasses (Hörz et al., 2002) that we have analyzed contain substantial Al and Si; none of them are pure carbonate melts.

The lithophile-element contents of some impact-melt particles are outside the ranges for Moenkopi and Kaibab rocks. For example, the adjusted La content of a few are higher than

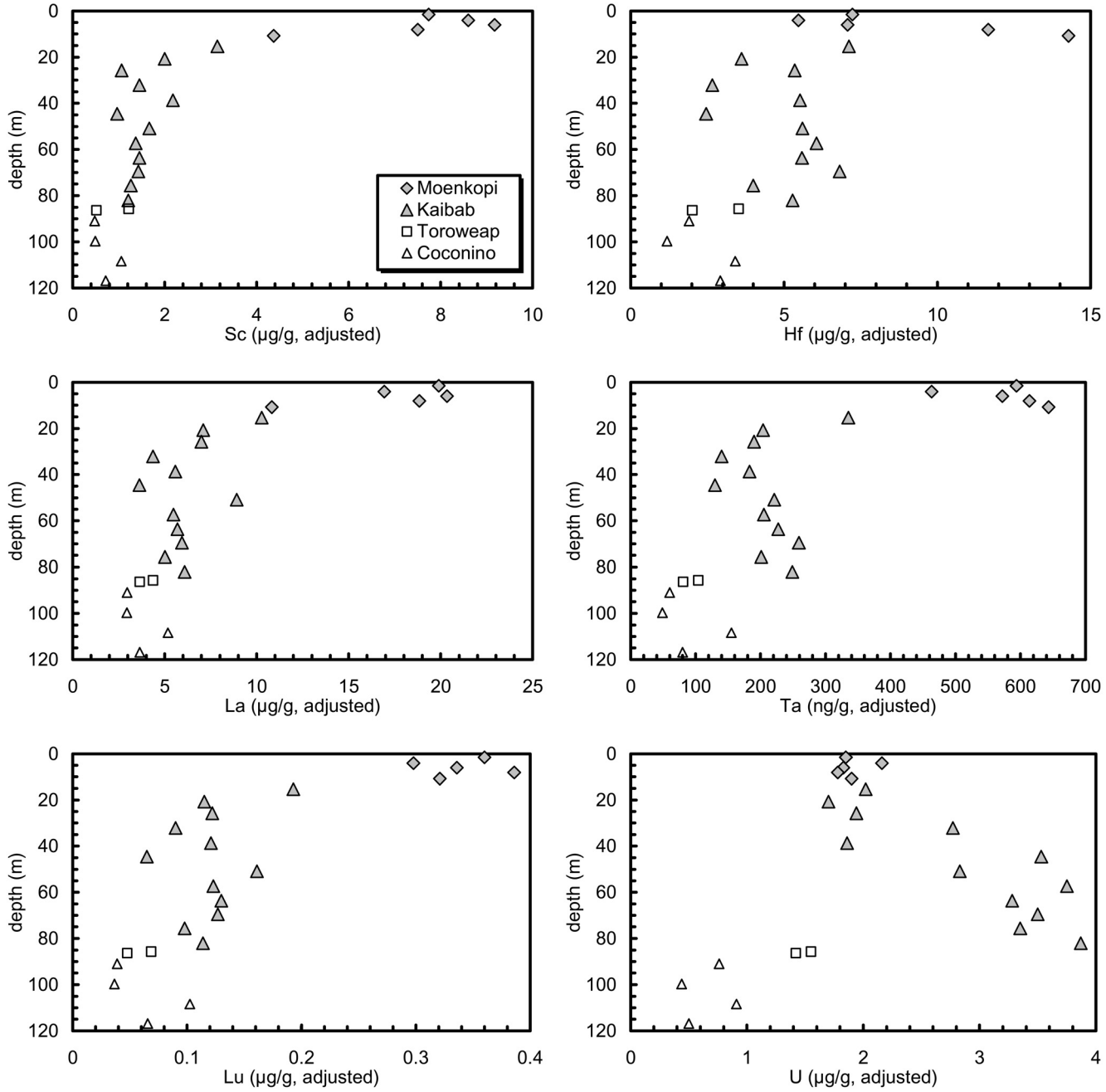

Figure 2. Variation in trace-element compositions of Meteor Crater target rocks with depth demonstrating the geochemical characteristics of the different formations.

observed in our suite of Moenkopi rocks, while the U and K contents of many are lower than those of Kaibab or Moenkopi rocks (Fig. 5). The high La contents determined for a few impact-melt particles likely indicates that our sampling of the Moenkopi formation at ~2.5 m scale was inadequate to fully define its compositional variations.

The low K and U contents for many impact-melt particles suggest possible fractionation during or after formation. Potassium could have been partially volatilized during the high temperature phase. Uranium is normally considered a refractory element, but some U halides are quite volatile (Lide, 2001). The Kaibab formation typically contains 1–2 µg/g Br (Table 2) and likely much higher Cl contents (seawater Cl/Br ~290). Hence, loss of species such as UCl_4 (boiling point 1064°K, Lide, 2001) may have occurred. Alternatively, the low K and U contents might indicate loss during low-temperature alteration of glasses in the particles.

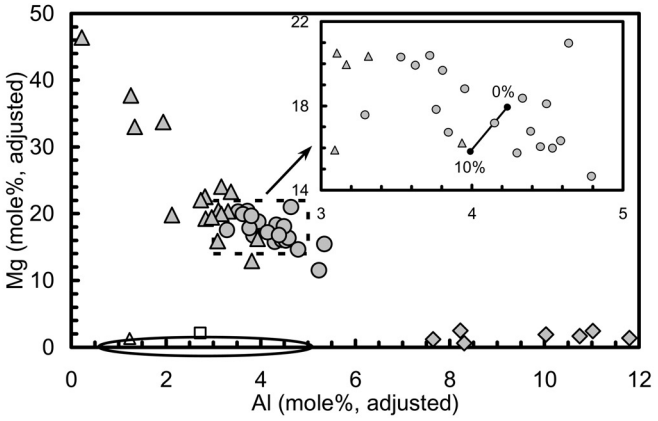

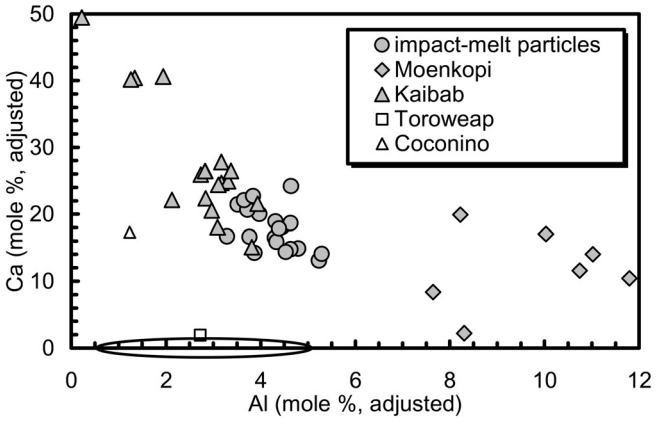

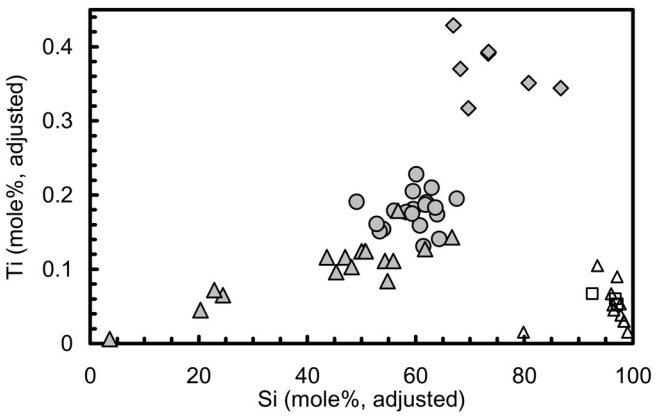

Figure 3. Major-element variation diagrams comparing Meteor Crater target rocks with impact-melt particles demonstrating that the Moenkopi and Kaibab Formations are the major target-rock components. The inset in the Mg vs. Al diagram shows that mixing of at most 10% of Coconino Formation could be hidden in the data scatter, but no Coconino or Toroweap components are required by the data. The ovals enclose Toroweap and Coconino samples with very low Mg and Ca contents. Some target-rock data from See et al. (2002).

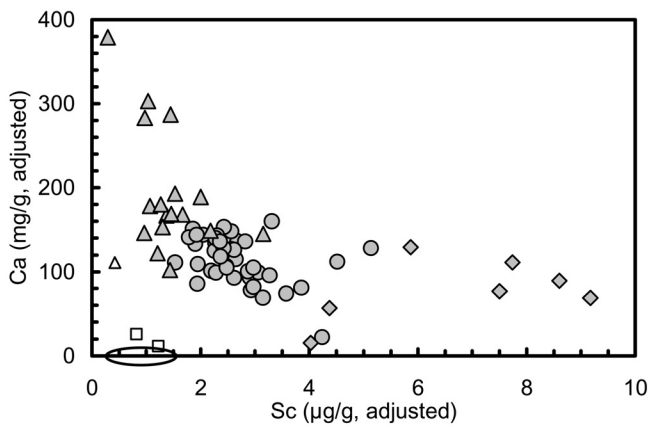

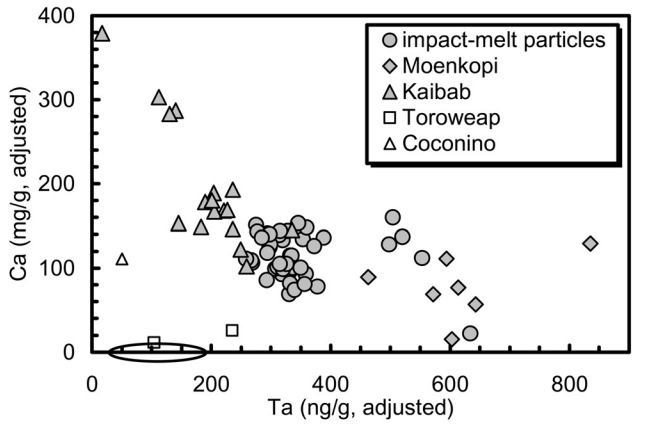

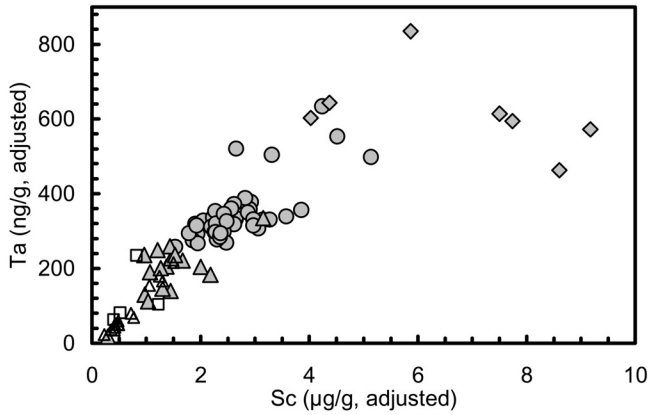

Figure 4. Ca vs. Sc, Ca vs. Ta, and Ta vs. Sc diagrams comparing Meteor Crater target rocks with impact-melt particles demonstrating that the Moenkopi and Kaibab Formations are the major target-rock components. The ovals enclose Toroweap and Coconino samples with very low Ca contents.

We documented late oxidation of Fe in glasses (Hörz et al., 2002), and interior vesicles in some impact-melt particles contain secondary phases indicating leaching from the particles. Uranium is subject to oxidation and mobilization during alteration, and alkali elements are typically easily mobilized. Regardless, the K and U contents of the impact-melt particles do not indicate that Toroweap or Coconino are significant components. Those impact-melt particles with K and U contents like those of Toroweap and Coconino rocks nevertheless contain high Ca contents demonstrating a dominant Kaibab component.

Based on the somewhat variable major-element compositions of glasses in impact-melt particles, we concluded that incomplete mixing rocks from the upper 30 m of the target formed many, if not most of them (Hörz et al., 2002). We have not attempted to do mixing calculations for bulk impact-melt particles presented here because the compositional ranges in the target rocks (Fig. 2) preclude unique solutions. We also concluded that the higher SiO_2 contents of some of the glasses *may* indicate a small component of Coconino is present, but this was not *required* by the data (Hörz et al., 2002). The major-element contents of the impact-melt particles would allow for as much as ~10% Coconino (Fig. 3). However, because all major- and trace-element data (excluding potentially mobile elements) for the impact-melt particles lie between the fields for Moenkopi and Kaibab, we believe it to be more plausible that only these two rock units were mixed in the melt zone to form the particles, and thus the melt zone extends no deeper than the base of the Kaibab, ~85 m.

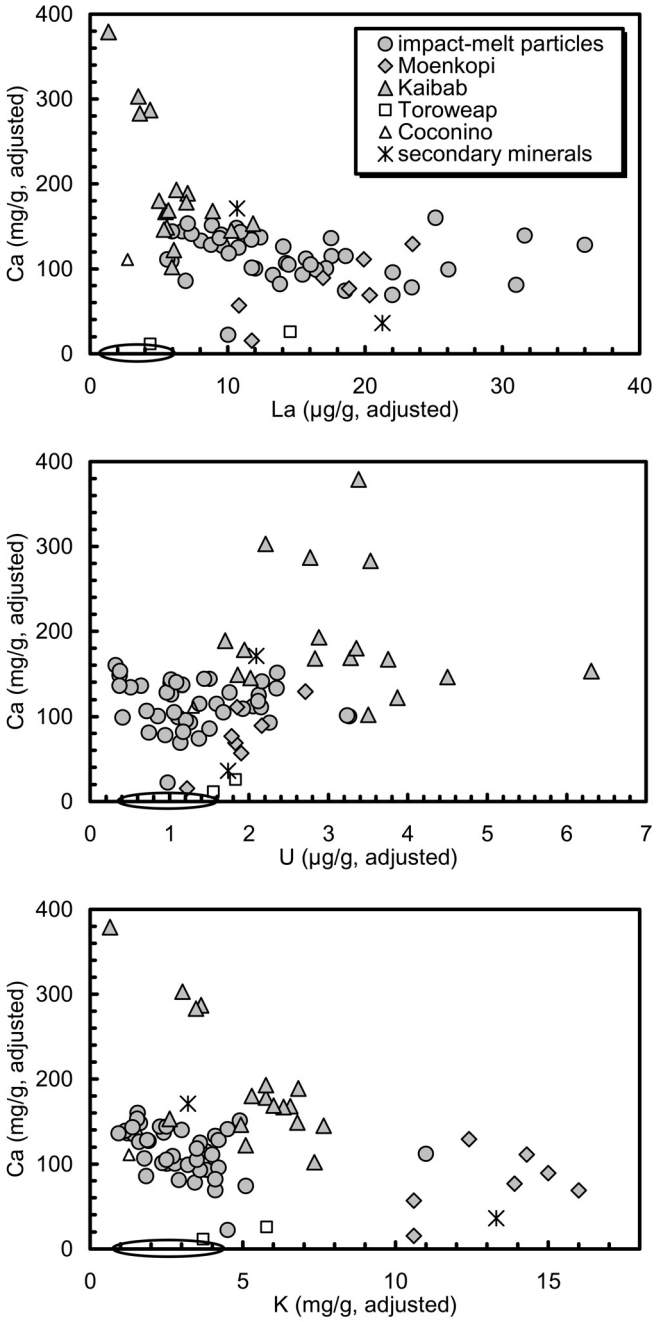

Figure 5. Ca vs. trace-element diagrams comparing Meteor Crater target rocks with impact-melt particles. The ovals enclose Toroweap and Coconino samples with very low Ca contents. Secondary mineral data are from Appendix 4.

Siderophile Elements and Projectile-Target Mixing

The impact-melt particles contain a substantial projectile component. Their Co, Ni, and Ir contents normalized to the mean Canyon Diablo metal composition (Appendix 1) reach 22%–27% that of the projectile (Fig. 6). However, CO_2 was volatilized from the carbonate-rich target rocks, and the actual maximum projectile component is less. There is a reasonably good correlation between target-rock CaO+MgO and LOI (See et al., 2002). We have used this to estimate the mass of target rock lost during impact melting for particles for which we have major-element data (Table 4, plus H11, Table 1). We estimate that between 7% and 15% of the mass was lost, and that the maximum projectile component based on Co, Ni, and Ir was between 20% and 22%. Using an average mass correction of 11%, we find that the impact-melt particles average 14% projectile component. This is higher than we found for ballistically dispersed impact-melt particles from Wabar Crater (Fig. 6), where average projectile components were ~7% and ~9% for large and small glass beads, with a maximum of ~17% for one small bead (Mittlefehldt et al., 1992). As was the case for lithophile elements, the impact-melt particles are quite heterogeneous in siderophile element contents (Fig. 6).

Few other craters have both impact melts and impactor preserved, and very few analyses of impact melts have been done. Attrep et al. (1991) found projectile components of ~4% and ~10% (based on Co and Ni) for two impact melts from Wolfe Creek Crater (Fig. 6), and <1% for three impact melts from Henbury Crater. The types of impact melts analyzed were not specified. The very low projectile component in the Henbury Crater samples most likely indicates that they represent massive-melt objects. We previously showed that large melt specimens (>100 g) from Wabar contain a much smaller projectile component than

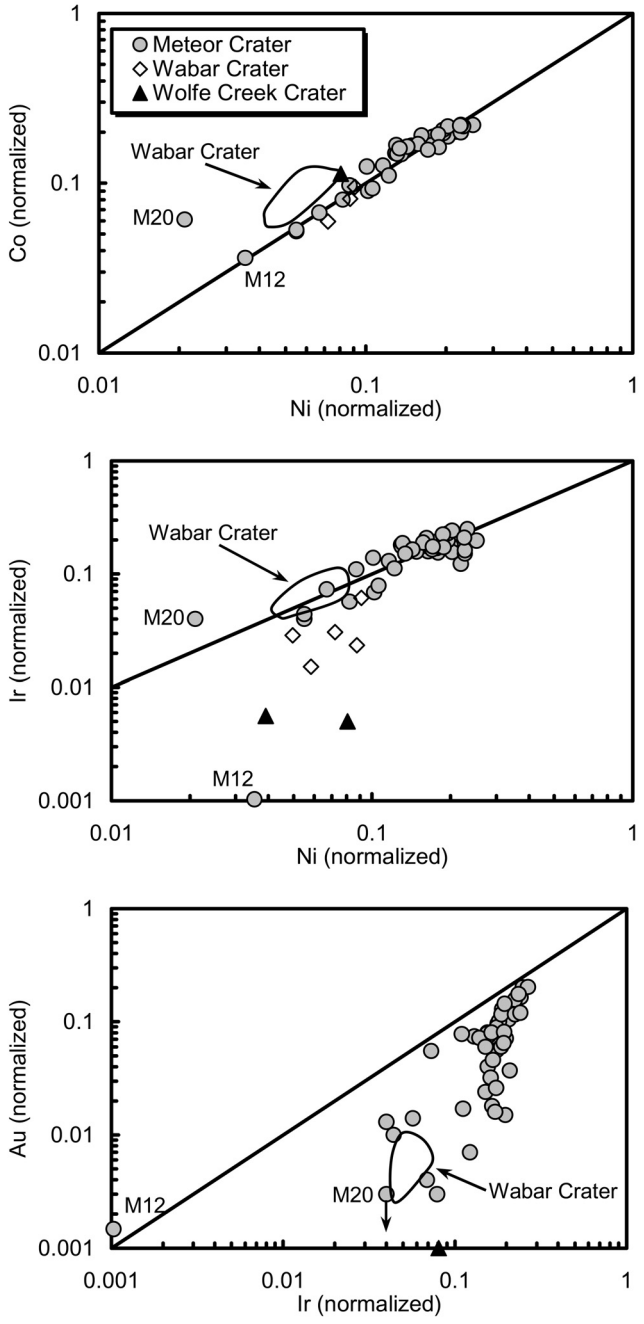

Figure 6. Element-element diagrams for siderophile elements in Meteor Crater impact-melt particles, with comparative data from Wabar Crater (Mittlefehldt et al., 1992) and Wolfe Creek Crater (Attrep et al., 1991). The data are normalized to projectile compositions. The Meteor Crater samples have Co/Ni and Ir/Ni ratios equivalent to the Canyon Diablo iron, but show strong fractionations in Au/Ir. Lines indicate Canyon Diablo element ratios. Arrow on M20 signifies Au is plotted at the 2σ upper limit. Fields enclose the majority of Wabar Crater samples; the few samples plotted have Co/Ni and/or Ir/Ni ratios distinct from the majority. See text.

do ballistically dispersed, mm-sized melt beads (Mittlefehldt et al., 1992). The Henbury samples will not be discussed further.

The Meteor Crater impact-melt particles have relatively unfractionated Co/Ni and Ir/Ni ratios, but Au is strongly fractionated as exemplified by Au/Ir ratios (Fig. 6). The Au fractionation is independent of the amount of projectile component in the particles. Samples with projectile-normalized Au/Ni ratios as low as 0.03 have normalized Co contents ~20% that of the Canyon Diablo iron, and two samples with normalized Au/Ni of 0.82 and 0.90 have normalized Co contents of 7% and 10% that of the projectile (Fig. 7). This shows that the Au fractionation is independent of the target-projectile mixing process, i.e., fractional condensation from a vapor cloud, or selective vaporization of siderophile elements from impact melts, is not the cause (see Gibbons et al., 1976; Kelly et al., 1974 for discussions of proposed fractionation processes). Hydrocode simulations of the Meteor Crater impact also show that for plausible impact velocities, projectile vaporization seems unimportant (Schnabel et al., 1999).

Two samples have anomalous siderophile-element characteristics. Particle M20 has high Co/Ni and Ir/Ni ratios due to depletion in Ni—its Ir/Co ratio is within the range of other impact-melt particles. Particle M20 contains clear glass and two types of altered glass intimately mixed (Hörz et al., 2002). The clear glass contains ~7% projectile component (total Fe as FeO, 8.43 wt%) and has an Fe/Ni ratio like that of the projectile, while the altered glasses are more iron-rich (total Fe as FeO, 11.1–14.2 wt%) with Fe/Ni ratios much greater than that of the Canyon Diablo iron (Hörz et al., 2002). The bulk sample of M20 studied here is like the clear glass in Fe content, but like the two types of altered glass in Na, K, and Ca. Possibly, the anomalous characteristics of M20 may simply reflect heterogeneous distribution of siderophile elements among different glass types. Particle M12 has a very low Ir/Ni ratio due to an anomalous Ir content. This particle has a Au/Ir ratio like that of Canyon Diablo, but this is anomalous compared to all other impact-melt particles with low Ir and Au contents (Fig. 6). Particle M12 contains only clear glass and the lowest projectile component found (Hörz et al., 2002). This is also observed in the bulk impact-melt particle, with ~3.5% projectile based on Co and Ni, but only ~0.1% based on Ir and Au (Fig. 6).

The siderophile-element characteristics of the Meteor Crater impact-melt particles show some similarities and some differences with those from Wabar and Wolfe Creek Craters (Fig. 6). Most Wabar samples have Co/Ni ratios significantly elevated above that of the impactor, while only Meteor Crater particle M20 is so endowed. The single Wolfe Creek Crater sample plots close to the impactor line. Most Wabar impact-melt particles have Ir/Ni ratios like that of the impactor. A few have anomalously low Ir/Ni ratios, but none are as anomalous as M12. Both Wolfe Creek Crater samples show anomalous Ir/Ni ratios, but again, not to the extent of M12. All samples from Wabar Crater and the single sample from Wolfe Creek Crater have Au/Ir ratios less than that of the projectile. Although only three craters have been sampled, with only a single Au determination for one, the

data suggest Au fractionation may be a common process occurring during formation of ballistically dispersed impact melts at terrestrial craters.

Attrep et al. (1991) and Mittlefehldt et al. (1992) noted that because siderophile-element ratios are fractionated at some terrestrial craters, attempts to identify impactor types from terrestrial and lunar impact melts should be treated cautiously. We still believe this to be true for terrestrial craters, but the observed fractionations may be uniquely terrestrial. There is a general tendency for those Meteor Crater impact-melt particles with the highest molar (Ca+Mg)/Si (highest Kaibab content) to have lower normalized Au/Ir ratios (Fig. 8). Kaibab samples have higher Br contents (Fig. 8), and Se, a proxy for S, was detected almost exclusively in Kaibab rocks (Table 2). The Au fractionation may be tied to the volatile content of the target, and thus loss of volatile Au complexes may have caused the fractionation. If true, then siderophile-element fractionation may not occur during impact melting on the volatile-poor Moon.

The case is not clear-cut; substantial scatter in the Meteor Crater data (Fig. 8) obscures compositional correlations. This may result from the heterogeneous nature of the Kaibab (Figs. 1 and 2; Hörz et al., 2002; See et al., 2002), the heterogeneous melting process, or signify that the trend is not real. Wolfe Creek Crater was formed in Precambrian quartzite, but we have no detailed compositional information on the target rocks. Wabar Crater was formed in sandstone. The low Ca contents of Wabar impact glasses and target materials indicate that there was little carbonate in the target (Hörz et al., 1989; Mittlefehldt et al., 1992). We do not have Br or Se data for the Wabar target-rock samples, and thus, cannot compare possible halogen or sulfate contents with Meteor Crater. Similar data sets from additional craters with preserved projectiles are needed to further evaluate the cause of Au fractionation.

We deduced that more projectile material was mixed into melts formed in the upper portions of the melt zone at Wabar crater (Mittlefehldt et al., 1992). The Meteor Crater data give some support to this. The Kaibab rocks have the highest molar (Ca+Mg)/Si and (Ca+Mg)/Al ratios among the target rocks (Fig. 9). These ratios should then increase in impact-melt particles formed as the melt zone penetrates deeper into the section. Impact-melt particles with (Ca+Mg)/Si and (Ca+Mg)/Al ratios less than or at the low end of the range for the Kaibab rocks have projectile-normalized Ir contents, on average, higher than those with the highest (Ca+Mg)/Si and (Ca+Mg)/Al ratios (Fig. 9). Those samples with higher (Ca+Mg)/Si and (Ca+Mg)/Al ratios had higher carbonate contents and have lost the most mass through CO_2 devolatilization. Thus, their normalized Ir contents have been enhanced more by this process than those with low (Ca+Mg)/Si and (Ca+Mg)/Al. The data are thus consistent with a generally decreasing projectile/target mixing ratio as the projectile penetrates. Samples with the highest normalized Ir contents have intermediate (Ca+Mg)/Si (~0.5–0.6) and (Ca+Mg)/Al (~7–8) ratios (Fig. 9), and may indicate that the peak projectile/target mixing ratio was reached at some intermediate depth.

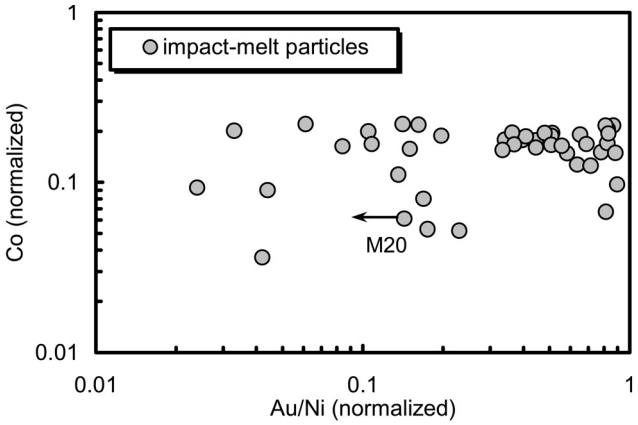

Figure 7. Co vs. Au/Ni for impact-melt particles. Particles covering nearly the entire rage in Au/Ni ratios can have similar Co contents, and samples with similar Au/Ni can have substantially different Co contents. Thus the Au/Ni fractionation is not related to the mixing ratio of projectile and target materials. Arrow on M20 signifies Au/Ni is plotted using the Au 2σ upper limit.

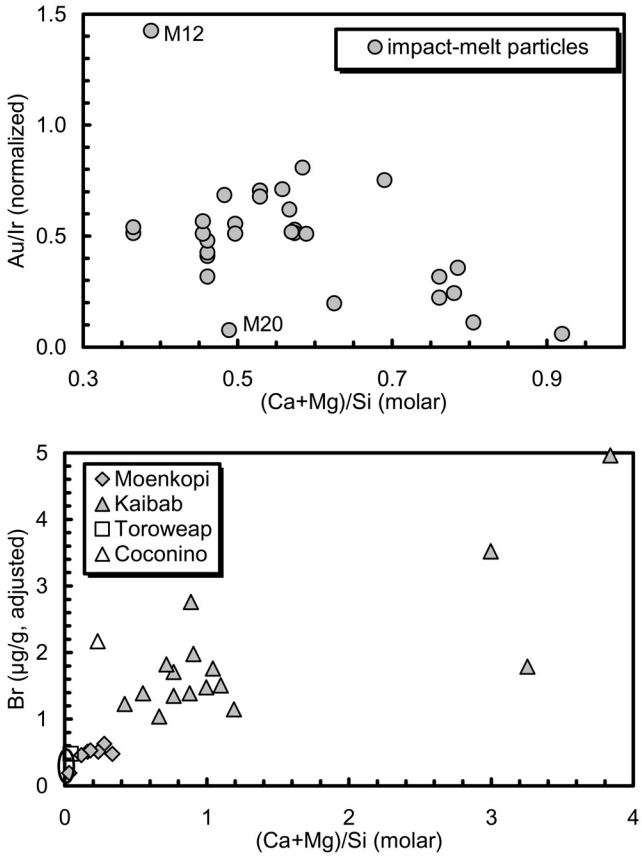

Figure 8. Au/Ir vs. (Ca+Mg)/Si of impact-melt particles shows that those particles with a high dolomite component tend to have lower Au/Ir ratios. Br vs. (Ca+Mg)/Si of target rocks show that the halide Br is roughly correlated with the dolomite content of the target rock. These suggest that volatilization of Au-halides may be responsible for the observed fractionation. Gold was below the detection limit in M20; its Au/Ir ratio was calculated using the Au 2σ upper limit. The oval encloses Toroweap and Coconino samples with very low Br contents.

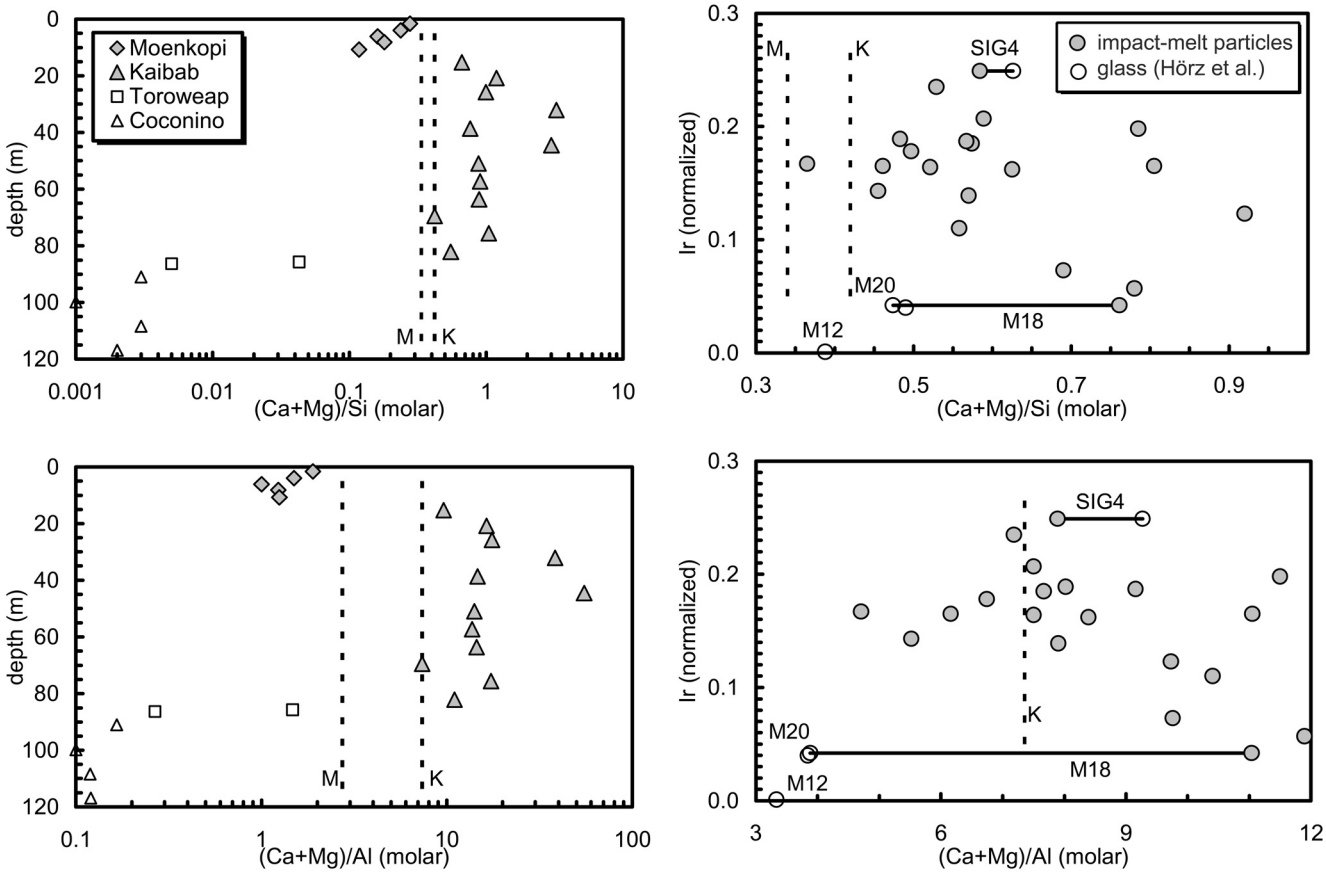

Figure 9. Variations in (Ca+Mg)/Si and (Ca+Mg)/Al with depth in target rocks (left) and with Ir content in impact-melt particles (right). Dashed lines labeled K mark the lower limits of (Ca+Mg)/Si and (Ca+Mg)/Al observed for Kaibab samples, while the line labeled M marks the upper limit of (Ca+Mg)/Si in Moenkopi samples—all Moenkopi samples have (Ca+Mg)/Al <3. Tie lines in right-side diagrams connect particles plotted using both bulk particle major element data (Table 4) and clear glass data (Hörz et al., 2002). See text.

Two impact-melt particles, M12 and M20, have lithophile-element contents indicating a higher Moenkopi component, yet have very low normalized Ir contents (Fig. 9), contrary to the general trend just discussed. The data for these are from clear glass analyses of Hörz et al. (2002); the samples were too small for bulk major element analysis. These authors inferred that the M12 and M20 glasses contained a higher Moenkopi component than most clear glasses, and that their low FeO contents indicated a low projectile component. Our data for K, Ca, and Fe on bulk M12 match well the clear glass data (Hörz et al., 2002, Table 3) suggesting that most of the bead was composed of such glass. As discussed above, M12 has anomalous siderophile-element contents compared to all other impact-melt particles. The bulk data for M20 do not match the glass data. Bulk particle M20 has the lowest CaO content (Table 3), yet the clear glass has among the highest (Hörz et al., 2002, Table 3). Altered glass in M20 has much lower CaO contents (Hörz et al., 2002), similar to what we found for the bulk particle. However, the altered glass has much higher Fe contents than the clear glass, and our bulk particle datum matches the clear glass. M20 also has somewhat anomalous siderophile-element contents (Fig. 6). Thus, M12 and M20 should be treated cautiously when attempting to infer projectile-target mixing details.

We have major-element compositions for bulk particles (Table 4) and clear glasses (Hörz et al., 2002) from M18 and SIG-4. Bulk SIG-4 has (Ca+Mg)/Al and (Ca+Mg)/Si very similar to those of the clear glass (Fig. 9). Bulk M18 is very different from its clear glass in major-element contents (Fig. 9). It contains higher CaO and MgO, and lower Al_2O_3 than does the clear glass, suggesting incorporation of dolomite clasts, an additional Kaibab component not present in the clear glass. Thus, it is difficult to determine whether M18 violates the projectile-target mixing generalization discussed above.

Hörz et al. (2002) showed that there are two basic types of glasses in the impact-melt particles: those with low Fe and Ni and Ni/Fe like that of the projectile, and those with high Fe, low Ni, and Ni/Fe much lower than that of the projectile. The bulk particles have a continuum of Fe contents covering the total range observed for glasses, but all have Ni/Fe like that of the impactor. Thus bulk impact-melt particles have variable contents of finely

disseminated, unfractionated (except for Au) projectile material. Some glasses on the other hand, contain a fractionated projectile component that must be compensated by other phases, probably metal or sulfide blebs, in the bulk particles. Electron microprobe analyses of metal blebs in impact-melt particles show that they can be highly enriched in Ni and Co relative to Canyon Diablo metal (Brett, 1967; Kelly et al., 1974; our unpublished data), and can balance the low Ni contents of pure glasses with low Ni/Fe observed by Hörz et al. (2002).

Metallic Spherules and Melting of the Projectile

Blau et al. (1973) studied a suite of metallic spherules from Meteor Crater. They concluded that the dendritic texture demonstrated that the spherules solidified by quenching of molten droplets, and that the textures of some are similar to those observed for Fe-Ni alloys containing C. They also noted that the spherules are enriched in Ni, S, and P compared to Canyon Diablo metal and suggested that this was due to slight selective melting of troilite-schreibersite-rich regions of the meteorite. Finally, Blau et al. (1973) argued that high Co contents of the spherules compared to Canyon Diablo metal was the result of oxidation of the spherules, enhancing the Ni and Co contents through loss of Fe oxide. This process also led to some oxidative loss of S and P (Blau et al., 1973).

In contrast, Kelly et al. (1974) noted that the S content of the spherules—9–28 mg/g (Blau et al., 1973)—is not enhanced relative to an estimated bulk meteorite S content of 22 mg/g, and that Ni/Co and Ni/Cu ratios are like those of the bulk meteorite. Kelly et al. (1974) concluded that the spherules were formed by melting bulk Canyon Diablo material, not selective melting of troilite-schreibersite-rich regions. Kelly et al. (1974) explained the high Ni, Co, and Cu contents relative to bulk meteorite by oxidation and removal of Fe.

Buchwald (1975, p. 392) estimated the bulk meteorite S content is ~9–10 mg/g, about half that estimated by Kelly et al. (1974) using older modal data. Thus the S content of the spherules may be enhanced by up to a factor of ~3 compared to the bulk meteorite. Buchwald (1975, p. 392) also estimates a bulk meteorite P content of 2.5 mg/g. The spherules contain 7–14 mg/g (Blau et al., 1973), suggesting they may be enriched up to ~6 times in P. This seems to support the contention of Blau et al. (1973) that some selective melting of troilite-schreibersite-rich regions occurred. However, Blau et al. (1973) did their analyses by electron microprobe using an "integrated line scan technique" on heterogeneous samples. True bulk spherule S and P contents need to be determined.

Figure 10 shows our metallic spherule data and those of Xue et al. (1995). Most spherules form a trend away from Canyon Diablo toward higher Ni but lower Fe, consistent with simple loss of Fe (arrow, upper panel). A few spherules plot below the Fe-loss trend. Either these samples contained some iron oxides–hydrous oxides that were not removed prior to analysis, or they are richer in C, P, and/or S than bulk Canyon Diablo. Note that the oxide-shell samples analyzed by Xue et al. (1995) plot at a lower normalized Fe abundance than "ideal" limonite ($FeO{\bullet}OH{\bullet}2.1H_2O$) and with higher Fe/Ni than the metal spherules they were taken from (tie lines). This is consistent with enrichment in Fe relative to the metallic core coupled with dilution by H, O, C, P, and/or S. Because the oxide shells have lower bulk Fe than "ideal" limonite, some dilution by C, P, and/or S is indicated.

Cobalt-Ni, Ir-Ni, and Au-Ni are well correlated in the spherules (Fig. 10). Kelly et al. (1974) argued that the Co/Ni ratios of the spherules were identical to the bulk metal of Canyon Diablo. We find subtle variations in siderophile-element/Ni ratios in the spherules. The Co-Ni trend has a slightly lower slope than the Canyon Diablo ratio, while Au/Ni has a slightly higher slope. Regression lines pass through the mean Canyon Diablo composition (Fig. 10). This is consistent with the oxidation model of Kelly et al. (1974). Cobalt is more readily oxidized than Ni. Those spherules with the highest Ni, having suffered the most oxidation and loss of Fe, have also experienced some oxidative loss of Co and have low Co/Ni ratios. Gold is less readily oxidized than Ni and shows the opposite—high Au/Ni for the most Ni-rich spherules.

Four spherules have Ni contents lower than bulk Canyon Diablo (numbers 12, 14, 17, 21; Table 5). They also have among the lowest sums of Fe, Co and Ni (Table 5), indicating that they contain larger amounts of diluents than do most other spherules. Finally, they have high Co/Ni and low Au/Ni ratios (Fig. 10). All of these characteristics are consistent with their containing a substantial amount of the Fe-rich, Ni-Au–poor oxides produced during spherule formation. One would expect the oxide to form on the outer surface of the spherule. Thus, should these four spherules be enriched in oxides, the Co-Ni-Ir-Au–rich metallic core of the spherule somehow was lost during formation.

All of the spherules have As/Ni ratios in excess of that of Canyon Diablo (Fig. 10), contrary to expectations. Arsenic is more easily oxidized than Ni and should be depleted relative to it, but Ni-rich spherules have As/Ni ratios of 1.89–2.79 times Canyon Diablo. The As-Ni data also scatter considerably compared to the very linear Co-Ni array (Fig. 10). Our As-Ni data closely mimic the P-Ni data of Blau et al. (1973) (Fig. 10), suggesting that the anomalous enrichment of As may be a result of slight selective melting of schreibersite-troilite–rich regions of the impactor. Arsenic and P are incompatible elements during crystallization of molten Fe-Ni, and will be correlated in irons (e.g., Scott, 1972). We did not find data on the As content of schreibersite, but As is in the same chemical group as P, suggesting that schreibersite exsolved from the metal may be enriched in As. The high As contents of the spherules may thus support slight selective melting of troilite-schreibersite-rich regions of Canyon Diablo as the explanation for enrichments in P and S.

Canyon Diablo contains graphite-troilite inclusions that are typically rimmed by schreibersite and cohenite (Buchwald, 1975). These inclusions have lower mean density than the surrounding metal. This will cause a passing shock front to reverberate (e.g., Kieffer, 1971), resulting in localized stress and temperature concentrations along metal-inclusion margins (e.g., Melosh,

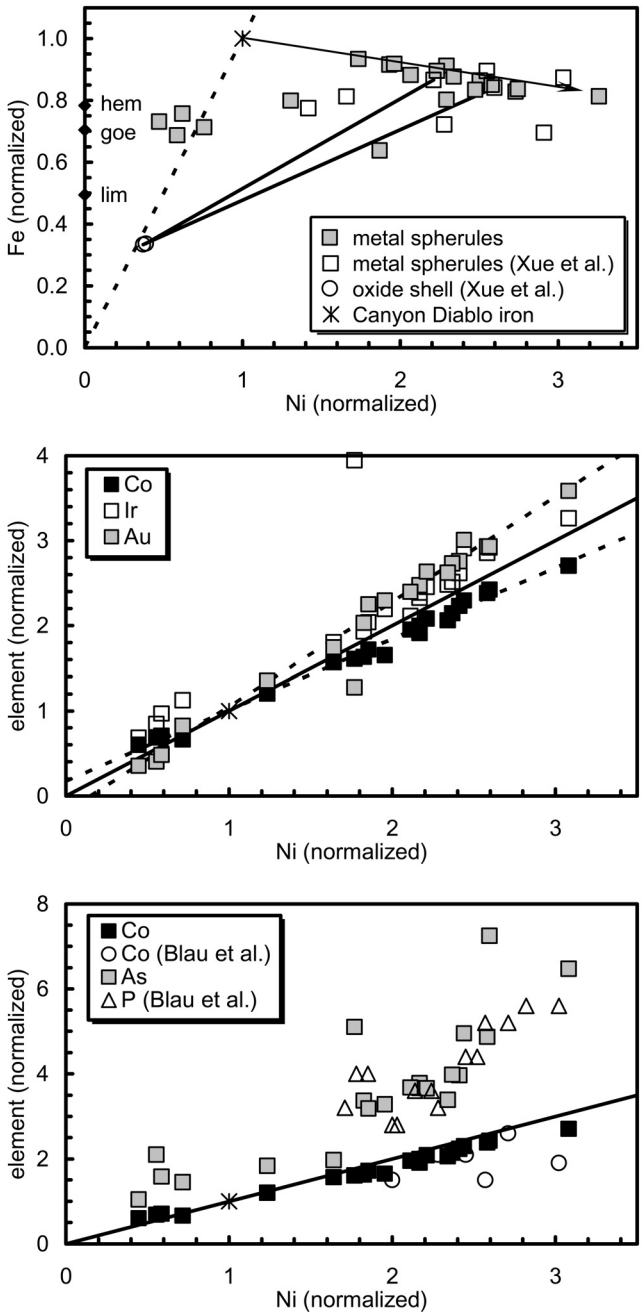

Figure 10. Siderophile-element data for metallic spherules compared to the Canyon Diablo iron. Most spherules have Fe and Ni contents that follow a trend of Fe loss (arrow, upper diagram). Some samples with low Fe are consistent with dilution by oxides. Equivalent normalized Fe contents for hematite, goethite and limonite are shown for comparison. Co-Ni, Ir-Ni and Au-Ni are highly correlated, with most samples enriched in these elements compared to the Canyon Diablo iron. Dashed lines are regression lines through the Co-Ni and Au-Ni data. The slopes of these lines are consistent with expectations from a simple oxidation model (see text). The metallic spherules show enrichments in As that are inconsistent with a simple oxidation model, but closely mimic the P-Ni trend. This suggests that some enhanced melting of graphite-troilite-schreibersite-rich regions of Canyon Diablo may have occurred (see text). Some data are taken from Blau et al. (1973) and Xue et al. (1995).

1989; Stöffler et al., 1991), leading to enhanced localized melting at metal-inclusion interfaces. Hydrocode simulations of the Meteor Crater impact show that this can occur along the trailing edge of the impactor at moderate shock pressures, i.e., moderate depths below the rear surface (Schnabel et al., 1999).

We conclude that both enhanced melting of graphite-troilite-schreibersite inclusions and oxidation and removal of Fe (and other elements) played roles in producing the chemical characteristics of the metallic spherules. Kelly et al. (1974) and we ground off the oxide coating on the spherules before analysis under the assumption these represented low-temperature rusting of the spherules. In retrospect, this most likely biased the data. The oxide coatings likely represent original high-temperature oxides produced as the spherules were airborne immediately after the impact. By grinding these off, we artificially increased the concentrations of the less oxidized elements that are concentrated in the metallic cores. True bulk analyses of spherules, including the oxide coatings, are needed to further evaluate their origin.

Geochemical Constraints on the Impact Process

We have shown that impact-melt particles contain material from the upper part of the target stratigraphy, that all are consistent with mixtures of Moenkopi and Kaibab rocks, and that those particles that seem to have been derived from lower portions of the melt zone contain less projectile material. These observations allow us to constrain the mechanism of impact melting.

One mechanism for producing dispersed impact-melts is through jetting, a process that occurs during the earliest phase of cratering when the free surface of a hypervelocity projectile forms an oblique angle with the target and results in target-projectile mixing (see Kieffer, 1977; Melosh, 1989). At Meteor Crater, this geometry occurred when a roughly spherical Canyon Diablo meteoroid contacted the target surface (Fig. 11), and continued until the projectile penetrated about halfway into the target (Melosh, 1989). Roddy (1978) calculated the kinetic energy of formation of Meteor Crater, and the projectile size for various assumed impact velocities. The lowest velocity assumed results in a maximum projectile radius of ~16 m, which sets the approximate maximum depth for jetting. We previously favored a shallow zone of melting for formation of some of the impact-melt glasses, <30 m (Hörz et al., 2002), compatible with jetting as the formation mechanism. However, none of the impact-melt particles (this study) or the clear glasses (Hörz et al., 2002) contains only Moenkopi and projectile components. Roddy (1978) estimated the Moenkopi averaged ~8.5 m thick in the target zone. We thus expect that some impact melts should be free of Kaibab material if jetting was a major formation mechanism. Because of this, we do not believe jetting was the dominant mechanism for production of the impact-melts. The bulk particles we have studied are mostly large, roughly cm-sized (Appendix 3). If jetting predominantly produced finer impact-melt spray, our studies could have missed those particles composed only of Moenkopi plus projectile. Thus we cannot rule out jetting as an important mechanism.

Another mechanism for formation of ballistically dispersed impact-melt particles is along the contact between the deforming projectile and the transient crater floor (Fig. 11). In this case, melting may extend to depths a few times the projectile radius (e.g., Melosh, 1989). Impact-melts produced would flow up the transient crater wall and could mix with solid target material during flow. Thus, melts formed after the deformed projectile was entirely below the original target surface would have the projectile component diluted by inclusion of clasts of target material. This is compatible with our data on bulk particles. Those particles with the lowest normalized Ir content (lowest projectile component) have the strongest Kaibab signature, suggesting formation deeper in the transient crater.

Because the melt compositions are variable, the melt-mixing process must have been chaotic, and clear signatures were not preserved in the impact-melt particles. We believe our data are compatible with both jetting and melting at the transient crater-deforming projectile interface as being important in the formation of the ballistically dispersed impact-melt particles at Meteor Crater.

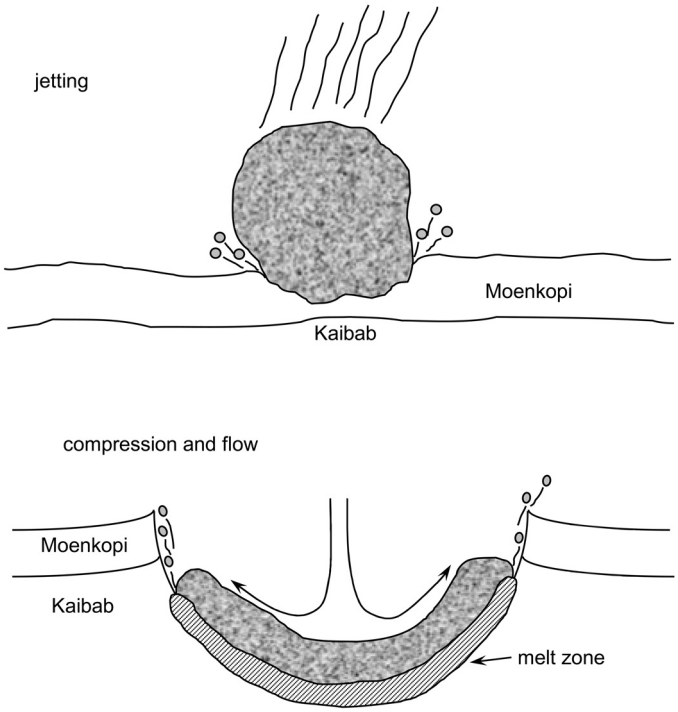

Figure 11. Schematic diagrams indicating two possible mechanisms for formation of impact-melt particles at Meteor Crater. Jetting (upper) occurs while the contact between the projectile and target remains at an oblique angle, and will continue until the projectile deforms substantially, roughly at a depth equal to its radius (Melosh, 1989). The thickness of the Moenkopi is estimated to have been ≥0.5 the projectile radius (Roddy, 1978). Thus jetting ought to have produced some impact-melt particles composed dominantly of Moenkopi plus meteorite. We have not found any of these, but the compositions of some melts indicate formation at shallow levels (<30 m) of the target (Hörz et al., 2002). Impact-melts will also form at the interface between the deforming projectile and the transient crater floor (lower), and the melt zone will extend a few projectile radii below the surface (Melosh, 1989). Flow of the melt up the transient crater wall will promote mixing. The data suggest that many of the particles were formed by this latter mechanism.

CONCLUSIONS

Ballistically dispersed impact-melt particles from Meteor Crater are heterogeneous in composition and are dominantly composed of three components: Canyon Diablo meteorite, Moenkopi Formation and Kaibab Formation. The compositions of the impact-melt particles do not require that rocks from the lower portions of the target section—the Toroweap and Coconino Formations—be mixed in. The data do not rule out up to 10% contribution from these rocks, but it is more plausible that these sandstones are not components.

The bulk impact-melt particles contain on average ~14% Canyon Diablo iron, with a maximum of 20%–22%. This is higher than we previously found for ballistically dispersed impact-melts from the much smaller Wabar Crater (Mittlefehldt et al., 1992). Siderophile-element ratios are essentially unchanged from those of the Canyon Diablo iron, except for Au. Many samples have Au/Ni and Au/Ir ratios much lower than those of the projectile. The lowest ratios are found for impact-melt particles with the highest Kaibab component. The Br contents of Kaibab rocks are higher than those for other target rocks, and we suggest that loss of volatile Au halides may have caused the fractionation.

Metallic spherules are generally enriched in Co, Ni, Ir, and Au compared to Canyon Diablo metal. Element/Ni ratios show subtle deviations from Canyon Diablo ratios that are inversely correlated with ease of oxidation of the element relative to Ni. We attribute this to partial oxidation of molten metal spherules during flight. Because we ground off oxide coatings from the spherules prior to analysis, our data are biased in favor of the metallic cores. The spherule compositions are consistent with slight enhanced melting of schreibersite-troilite–rich regions of the projectile, and this can be explained by enhanced shock melting of lower density graphite-troilite-schreibersite inclusions present in Canyon Diablo.

ACKNOWLEDGMENTS

This paper is dedicated to the memory of David J. Roddy, field-guide, colleague, and friend.

We thank The Barringer Crater Company for permission to do field work in Meteor Crater, and the late D.J. Roddy for guiding our field collection. The senior author thanks J.H. Jones and A.H. Treiman for accompanying him in the field. We thank C.B. Moore and the Center for Meteorite Studies, Arizona State University, for providing the impact-melt particles and metallic spherules studied here. Reviews by H. Huber and an anonymous reviewer, and the editorial handling by A. Deutsch led to substantial improvements. The NASA Cosmochemistry Program supported DWM, and the Planetary Geology and Geophysics Program supported FH in these studies.

APPENDIX 1. CANYON DIABLO METEORITE

TABLE A1. AVERAGE COMPOSITION OF THE METAL PHASE OF CANYON DIABLO IRON METEORITE AND KEY ELEMENT RATIOS*

Cr	µg/g	25
Fe	mg/g	922
Co	µg/g	4660
Ni	mg/g	70.1
Ga	µg/g	81.8
Ge	µg/g	327
As	µg/g	13.1
Sb	ng/g	290
W	ng/g	1110
Ir	ng/g	2320
Au	ng/g	1560
Fe/Ni		13.2
Co/Ni		6.65×10^{-2}
Ir/Ni		3.31×10^{-5}
Au/Ni		2.23×10^{-5}
Au/Ir		0.672

*Average composition is taken from Choi et al. (1995) except for Fe. Iron is determined by difference from 1000 mg/g by subtracting Co and Ni from above, and C (1.6 mg/g) and P (2.0 mg/g) estimated from Buchwald (1975).

APPENDIX 2. TARGET ROCKS

Samples K-1, K-2, and C-1 through C-4 (Table 2) are representative samples of Kaibab and Coconino collected by Hörz from undocumented locations. Samples labeled Ma, Ka, Ta, Ca, etc., are from a continuous stratigraphic section collected by Hörz and See for this study (See et al., 2002). The samples described below were collected by Mittlefehldt from the crater and its vicinity.

Moenkopi Formation

MC-01: Light pink, massive sandstone; north crater wall, ~2–2.5 m above Kaibab contact.

MC-07: Reddish siltstone/clay-rich facies; block in talus, southwest crater wall.

Kaibab Formation

MC-06: Shattered gray dolomite; southwest crater wall, ~15 m above formation base.

MC-10: Gray dolomite; overturned flap, west crater rim.

MC-12: Gray dolomite; boulder float in stream, Oak Creek Canyon.

Toroweap Formation

MC-08: Gray sandstone; overturned flap, southwest crater rim.

MC-13: Knobby gray sandstone; overturned flap; southwest crater rim.

Coconino Formation

MC-02: White, frothy, and powdery sandstone fallback deposit; shaft dump, crater floor.

MC-03: Shattered gray sandstone; southwest crater wall, ~70 m below Kaibab.

MC-04: Clast-free gray matrix of brecciated sandstone; ~10 m above MC-03.

MC-05: Gray sandstone; southwest crater wall, ~5 m below Kaibab.

MC-09: Highly shocked sandstone ejecta debris; south crater rim.

MC-11: Gray sandstone; stream cut, Oak Creek Canyon.

APPENDIX 3. IMPACT-MELT PARTICLES

H11: Composite of 15 individual irregularly shaped cm-sized impact-melt particles. The particles are vesicular, with dark gray interiors and thin brownish rims. The particles were individually ground and the powders mixed and homogenized to produce a bulk sample of about 4 grams.

H11a: Individual cm-sized irregularly shaped impact-melt particle from the same group used to prepare H11.

IIG-1: Irregularly shaped dark brown vesicular impact-melt particle ~1.8 × 1.3 × 1.3 cm in size. Vesicles are up to ~4 mm in size. Numerous small clasts are present. Some secondary minerals are present on the surface and in interior vesicles. IIG-1a and IIG-1b were hand-picked from the freshest material.

IIG-2: Irregularly shaped dark brown impact-melt particle ~1.8 × 1.4 × 1.4 cm in size containing very few vesicles, ~1–2 mm in size. Numerous small clasts are present. Some secondary minerals are present on the surface and in interior vesicles. IIG-2a and IIG-2b were hand-picked from the freshest material.

IIG-3: Irregularly shaped dark brown impact-melt particle ~1.9 × 1.1 × 1.1 cm in size containing few vesicles ≤1 mm in size. Little clastic material is present. Some secondary minerals occur on the surface and in interior vesicles. Samples IIG-3a through IIG-3d were hand-picked from the freshest material.

IIG-4: Smooth, highly irregularly shaped impact-melt particle. The particle is composed of black to red-black glass and yellow-brown, melted clastic debris. The interior is cored with melted clastic material. Nearly pure impact-glass (IIG-4) and clast (IIG-4c) samples were hand-picked.

M1: Large (7 mm) accretionary sphere of black glass with many accretionary promontories and splashes, some flattened and transitional to the dark matrix glass. The bead is vesicular, almost a hollow shell. Some interior surfaces and small vesicles contain fine-grained secondary minerals.

M2: Large (5 × 3 mm), dense, black, shiny spheroid with sugary surface texture. It contains no prominent accretions, but has one hemispherical depression. The bead is very magnetic, and is an oxide bead.

M3: Large (9 mm) rounded brownish bead. The interior is highly porous and weathered with a distinctly orange, oxidized skin. The exterior surface is dull and pitted with sugary appearance. Quartz clasts are present. Samples M3a and M3b are two different samples of hand-picked material.

M4: Large (8 mm) ellipsoid of dark glass with grayish hue. It is a mixture of dark glass and a lighter grayish glass. Many accretionary particles are present. The interior is vesicular, nearly hollow, and contains secondary minerals. A patch of fine-grained, white sugary material may be a glassy clast. Sample M4a is hand-picked, glassy material; M4b is hand-picked material enriched in secondary minerals.

M5: Stubby ellipsoid (4 mm) of dark colored, fresh-appearing glass. The surface is dull and sugary with many small pits. The interior is very porous, essentially frothy. Accretionary features are abundant. Interior vesicles contain some secondary minerals.

M6: Large (12 mm), broken, ropy, and cylindrical lapillus of dull glass with pitted surface with many accretionary particles on the surface. Few clasts are present. The interior displays a dark, very porous glass matrix and tan inclusions of melt or finely crystalline material.

M7: Round sphere (3 mm) of dark glass with numerous accretionary beads. Slightly lighter colored glass makes distinct promonto-

ries. The interior contains numerous microscopic pores, some clasts, and a small amount of fine-grained secondary minerals.

M8: A highly porous, slag-like, very friable weathered brown glass containing numerous clasts and pockets of different colored melts. The rim is modestly oxidized. Sample M8a is hand-picked coarse fragments; M8b is the fine debris produced during crushing.

M10: A dull, dark colored impactite. It is coarsely porous and somewhat weathered with an oxidized rim, but only a small amount of fine-grained secondary minerals.

M11: A large (12–15 mm) flattened ellipsoid of porous, tan melt. The surface is unusually sculptured with polygons forming a cauliflower-like texture. The sample is highly altered.

M12: An unusual particle of tektite-like, dense black glass; almost volcanic in appearance. The sample is very fresh, and clast-poor; possibly clast-free.

M13: A very large (14 mm) aerodynamically shaped impactite of rusty-brown colored glass. The surface is dull and sugary in appearance with no good accretionary features. The interior is frothy and has a red colored weathering rind surrounding a dark gray/black core. Sample M13a is reddish rind glass; M13b is black interior glass.

M14: A large (8 mm long) elongated, ropy lapillus fragment. The surface has numerous weathered knobs of dull, secondary material and some clasts. The interior is frothy, containing dark and honey-yellow glass with little clastic material.

M15: A large, ropy lapillus fragment (~15 mm long) with many accretionary features of dark glass. Some secondary minerals are present on the surface. The interior shows yellowish weathering rind glass with a fresh black glass core. Some clastic material is present. The sample was very tough to break.

M16: A distinctly rusty-colored, highly porous aerodynamically shaped melt object. Most of the particle is altered, with little fresh, dark gray to black glass in the interior. It contains some clastic quartz.

M17: A large (11 mm) ropy, elongate lapillus of dense dark melt with many accretionary knobs on the surface. The interior includes fresh black glass and reddish, altered glass.

M18: A large ovoid lapillus (16 mm) with a grayish-white surface of secondary minerals and bleached glass. Numerous honey-colored pockets are visible. The interior displays intimate mixing of the different colored glasses. The particle contains a distinct, bleached rind. Sample M18a is hand-picked interior glass containing some bleached glass; M18b is enriched in bleached glass; M18c is exterior material enriched in secondary minerals.

M19: A flat, pancake shaped object displaying prominent ridges showing material flow and aerodynamic shaping. The interior is porous, somewhat weathered black glass with distinctly rusty-colored oxidation rim. Secondary minerals are present on the exterior.

M20: Small irregular fragment of a ballistic bead of dense mostly honey-colored glass.

M21: A very fresh appearing bead of yellow glass with accretionary promontories of black and yellow glasses—a mixed melt. No secondary minerals are present.

M22: A hollow hemisphere—a fragment of a hollow sphere—with a smooth outer surface. The interior glass is dark and contains numerous microvesicles.

M23: An elongate bead of yellow glass with prominent accretionary knobs. Some black glass is present in the interior.

M24: A large (9 × 2 mm) dumbbell of relatively dense, dark glass, somewhat sugary, and with a pitted surface. A very thin weathering rind is present.

M25: A fresh, small (3–4 mm) bead of dark glass with a distinctly shiny surface with an uneven distribution of accretionary features. The interior contains some vesicles, and a few clasts.

M26: A cylindrical object of unusual dark wine-red color. The particle is fresh with shiny surfaces and no prominent accretionary features. The interior contains some black glass.

M27: A sphere of very fresh dense dark glass with a smooth, shiny surface, fresh, dark, frothy glass in the interior, and with a thin alteration rind.

SIG-1: An oblong hollow spheroid ~5 × 4 × 4 mm in size with few protuberances. One end contains many <1 mm size vesicles. The interior cavity is filled with secondary minerals. Several fresh, black glass fragments were hand-picked for analysis.

SIG-2: A hollow sphere ~4 mm in size with a few protuberances and many <0.5 mm size vesicles. This sample contained relatively little secondary material. One piece of fresh glass was hand-picked for analysis.

SIG-3: Flattened (on one side) spheroid ~5 mm in size with a large protuberance on the flattened side. There are a few <1 mm size vesicles. This sample was partially hollow—a clast occupies part of the center. Fragments of impact glass (SIG-3) and a sample of secondary minerals (SIG-3w) were selected for analysis.

SIG-4: Slightly vesicular, smooth, brown, hollow glass ball. A red-brown weathering rind surrounds fresh black glass. The interior cavity is small, and partially filled with white secondary minerals.

APPENDIX 4. INAA DATA ON MISCELLANEOUS SAMPLES

TABLE A2. COMPOSITIONS OF MISCELLANEOUS SAMPLES FROM METEOR CRATER DETERMINED BY INSTRUMENTAL NEUTRON ACTIVATION ANALYSIS

		IIG-4c clast‡		SIG-3w sec min‡		M4b sec min‡		M18c sec min‡		M2 oxide‡	
mass†	mg	16.73	±	3.99	±	1.05	±	20.91	±	54.58	±
Na	µg/g	324	4	1800	20	169	4	1010	10	12.6	0.8
K_2O	wt%	0.91	0.02	1.25	0.03			0.28	0.01	0.014	0.007
CaO	wt%	18	1	3.9	0.5	50	2	17.4	0.6		
Sc	µg/g	4.05	0.05	4.25	0.05	0.12	0.01	2.11	0.02	0.11	0.03
Cr	µg/g	46	1	34	2			56.7	0.9	15	1
Fe	mg/g	54.6	0.6	13.2	0.4	2.1	0.2	56.5	0.6	712	7
Co	µg/g	213	2	18.0	0.2	15.6	0.3	254	3	2730	30
Ni	mg/g	3.27	0.08	0.11	0.02	0.2	0.1	3.53	0.07	14.1	0.3
Zn	µg/g							23	3		
As	µg/g	3.15	0.08	3.0	0.2	2.6	0.3	3.3	0.1	0.9	0.2
Br	µg/g	0.48	0.05	1.3	0.2	28	1	2.4	0.1		
Rb	µg/g	28	4	42	5			11	2		
Sr	µg/g			120	60			350	20		
Zr	µg/g	260	40	450	60			240	30		
Sb	ng/g	220	20	480	40			210	10		
Cs	µg/g	2.39	0.06	2.76	0.08			0.85	0.03		
Ba	µg/g	690	20	310	30	1000	200	3440	80		
La	µg/g	14.2	0.2	16.6	0.2	4.4	0.1	7.77	0.09	0.35	0.01
Ce	µg/g	28.0	0.5	29.6	0.8			16.2	0.3		
Nd	µg/g	12	3					9	3		
Sm	µg/g	3.04	0.04	2.72	0.04	0.51	0.03	1.62	0.02	0.053	0.005
Eu	µg/g	0.65	0.02	0.54	0.02			0.377	0.009		
Tb	µg/g	0.42	0.03	0.38	0.04			0.24	0.01		
Yb	µg/g	1.60	0.04	1.49	0.08			0.94	0.03		
Lu	µg/g	0.245	0.008	0.22	0.02	0.10	0.05	0.145	0.008		
Hf	µg/g	7.5	0.2	12.2	0.3			7.0	0.1		
Ta	ng/g	480	40	470	40			300	20		
W	ng/g	380	80	1100	300					700	300
Ir	ng/g	38	3					92	2		
Au	ng/g	4.7	0.7			24	9	10.9	0.9	33	2
Th	µg/g	4.0	0.1	4.3	0.2			2.10	0.06		
U	µg/g	1.56	0.06	1.4	0.1			1.52	0.06		

Note: In this table, Ni is given in units of mg/g. Individual uncertainties are given in the ± columns.
†Mass refers to mass in mg of analyzed material and represents most or all of the mass of sample prepared.
‡Clast—lithic clast separated from impact melt particle IIG-4; sec min—secondary minerals found in impact melt particles SIG-3, M4 and M18; oxide-rounded oxide bead.

REFERENCES CITED

Attrep, M., Jr., Orth, C.J., Quintana, L.R., Shoemaker, C.S., Shoemaker, E.M., and Taylor, S.R., 1991, Chemical fractionation of siderophile elements in impactites from Australian meteorite craters [abs.]: Lunar and Planetary Science, v. 22, p. 39–40.

Benedix, G.K., McCoy, T.J., Keil, K., and Love, S.G., 2000, A petrologic study of the IAB iron meteorites: Constraints on the formation of the IAB-Winonaite parent body: Meteoritics & Planetary Science, v. 35, p. 1127–1141.

Blau, P.J., Axon, H.J., and Goldstein, J.I., 1973, Investigation of the Canyon Diablo metallic spheroids and their relationship to the breakup of the Canyon Diablo meteorite: Journal of Geophysical Research, v. 78, p. 363–374.

Boyd, F.R., and Mertzman, S.A., 1987, Composition and structure of the Kaapvaal lithosphere, southern Africa, *in* Mysen, B.O., ed., Magmatic Processes: Physicochemical Principles: University Park, Pennsylvania, Geochemical Society, p. 13–24.

Brett, R., 1967, Metallic spherules in impactite and tektite glasses: American Mineralogist, v. 52, p. 721–733.

Brown, R.W., 1977, A sample fusion technique for whole rock analysis with the electron microprobe: Geochimica et Cosmochimica Acta, v. 41, p. 435–438.

Buchwald, V.F., 1975, Handbook of Iron Meteorites: Berkeley, University of California Press, 1418 p.

Bunch, T.E., Keil, K., and Olsen, E., 1970, Mineralogy and petrology of silicate inclusions in iron meteorites: Contributions to Mineralogy and Petrology, v. 25, p. 297–340.

Choi, B.-G., Ouyang, X., and Wasson, J.T., 1995, Classification and origin of IAB and IIICD iron meteorites: Geochimica et Cosmochimica Acta, v. 59, p. 593–612, doi: 10.1016/0016-7037(94)00384-X.

Dence, M.R., 1971, Impact melts: Journal of Geophysical Research, v. 76, p. 5552–5556.

Gibbons, R.V., Hörz, F., Thompson, T.D., and Brownlee, D.E., 1976, Metal spherules in Wabar, Monturaqui, and Henbury impactites: Proceedings, Lunar Science Conference, 7th, New York: New York, Pergamon Press, p. 863–880.

Grieve, R.A.F., 1982, The record of impact on Earth: Implications for a major Cretaceous/Tertiary impact event, *in* Silver, L.T., and Schultz, P.H., eds., Geological implications of impacts of large asteroids and comets on the earth: Geological Society of America Special Paper 190, p. 25–37.

Grieve, R.A.F., 1991, Terrestrial impact: The record in the rocks: Meteoritics, v. 26, p. 175–194.

Hagerty, J.J., and Newsom, H.E., 2003, Hydrothermal alteration at the Lonar Lake impact structure, India: Implications for impact cratering on Mars: Meteoritics & Planetary Science, v. 38, p. 365–381.

Hörz, F., See, T.H., Murali, A.V., and Blanchard, D.P., 1989, Heterogeneous dissemination of projectile materials in the impact melts from Wabar crater, Saudi Arabia: Proceedings, 19th Lunar and Planetary Science Conference: Houston, Lunar and Planetary Institute, p. 697–709.

Hörz, F., Mittlefehldt, D.W., See, T.H., and Galindo, C., 2002, Petrographic studies of the impact melts from Meteor Crater, Arizona, USA: Meteoritics & Planetary Science, v. 37, p. 501–531.

Kargel, J.S., Coffin, P., Kraft, M., Lewis, J.S., Moore, C., Roddy, D., Shoemaker, E.M., and Wittke, J.H., 1996, Systematic collection and analysis of meteoritic materials from Meteor Crater, Arizona [abs.]: Lunar and Planetary Science, v. 27, p. 645–646.

Kelly, W.R., Holdsworth, E., and Moore, C.B., 1974, The chemical composition of metallic spheroids and metallic particles within impactite from Barringer Meteorite Crater, Arizona: Geochimica et Cosmochimica Acta, v. 38, p. 533–543, doi: 10.1016/0016-7037(74)90039-8.

Kieffer, S.W., 1971, Shock metamorphism of the Coconino Sandstone at Meteor Crater, Arizona: Journal of Geophysical Research, v. 76, p. 5449–5473.

Kieffer, S.W., 1977, Impact conditions for formation of melt by jetting in silicates, *in* Roddy, D.J., Pepin, R.O., and Merrill, R.B., eds., Impact and Explosion Cratering: New York, New York, Pergamon Press, p. 751–769.

King, D.T., Jr., Neathery, T.L., Petruny, L.W., Koeberl, C., and Hames, W.E., 2002, Shallow-marine impact origin of the Wetumpka structure (Alabama, USA): Earth and Planetary Science Letters, v. 202, p. 541–549, doi: 10.1016/S0012-821X(02)00803-8.

Lide, D.R., ed., 2001, CRC Handbook of Chemistry and Physics, 82nd Edition: Boca Raton, Florida, CRC Press.

Melosh, H.J., 1989, Impact Cratering: A Geologic Process: New York, Oxford University Press, 245 p.

Mertzman, S.A., 2000, K-Ar results from the southern Oregon-northern California Cascade Range: Oregon Geology, v. 62, p. 99–122.

Mittlefehldt, D.W., and Lindstrom, M.M., 1991, Generation of abnormal trace element abundances in Antarctic eucrites by weathering processes: Geochimica et Cosmochimica Acta, v. 55, p. 77–87, doi: 10.1016/0016-7037(91)90401-P.

Mittlefehldt, D.W., and Lindstrom, M.M., 1993, Geochemistry and petrology of a suite of ten Yamato HED meteorites: Proceedings, National Institute of Polar Research Symposium on Antarctic Meteorites 17th, no. 6, p. 268–292.

Mittlefehldt, D.W., See, T.H., and Hörz, F., 1992, Dissemination and fractionation of projectile materials in the impact melts from Wabar Crater, Saudi Arabia: Meteoritics, v. 27, p. 361–370.

Mittlefehldt, D.W., McCoy, T.J., Goodrich, C.A., and Kracher, A., 1998, Nonchondritic meteorites from asteroidal bodies, *in* Papike, J.J., ed., Planetary Materials: Reviews in Mineralogy, v. 36, p. 4-1–4-195.

Mittlefehldt, D.W., Hörz, F., and See, T.H., 2000, Trace element chemistry of Meteor Crater impact-melt particles and target rocks—Empirical evidence on the cratering process [abs.]: Lunar and Planetary Science v. 31, no. 1798.

Morgan, J.W., Higuchi, H., Ganapathy, R., and Anders, E., 1975, Meteoritic material in four terrestrial meteorite craters: Proceedings, Lunar Science Conference, 6th, New York: New York, Pergamon Press, p. 1609–1623.

Nininger, H.H., 1956, Arizona's Meteorite Crater: Denver, Colorado, World Press, 232 p.

Nishiizumi, K., Kohl, C.P., Shoemaker, E.M., Arnold, J.R., Klein, J., Fink, D., and Middleton, R., 1991, In situ ^{10}Be-^{26}Al exposure ages at Meteor Crater, Arizona: Geochimica et Cosmochimica Acta, v. 55, p. 2699–2703, doi: 10.1016/0016-7037(91)90388-L.

Palme, H., 1982, Identification of projectiles of large terrestrial impact craters and some implications for the interpretation of Ir-rich Cretaceous/Tertiary boundary layers, *in* Silver, L.T., and Schultz, P.H., eds., Geological implications of impacts of large asteroids and comets on the earth: Geological Society of America Special Paper 190, p. 223–233.

Palme, H., Janssens, M.-J., Takahashi, H., Anders, E., and Hertogen, J., 1978, Meteoritic material at five large impact craters: Geochimica et Cosmochimica Acta, v. 42, p. 313–323, doi: 10.1016/0016-7037(78)90184-9.

Phillips, F.M., Zreda, M.G., Smith, S.S., Elmore, D., Kubik, P.W., Dorn, R.I., and Roddy, D.J., 1991, Age and geomorphic history of Meteor Crater, Arizona, from cosmogenic ^{36}Cl and ^{14}C in rock varnish: Geochimica et Cosmochimica Acta, v. 55, p. 2695–2698, doi: 10.1016/0016-7037(91)90387-K.

Roddy, D.J., 1978, Pre-impact geologic conditions, physical properties, energy calculations, meteorite and initial crater dimensions and orientations of joints, faults and walls at Meteor Crater, Arizona: Proceedings, Lunar and Planetary Science Conference, 9th, New York: New York, Pergamon Press, p. 3891–3930.

Roddy, D.J., Boyce, J.M., Colton, G.W., and Dial, A.L., Jr., 1975, Meteor Crater, Arizona, rim drilling with thickness, structural uplift, diameter, depth, volume, and mass-balance calculations: Proceedings, Lunar Science Conference, 6th, New York: New York, Pergamon Press, p. 2621–2644.

Schnabel, C., Pierazzo, E., Xue, S., Herzog, G.F., Masarik, J., Cresswell, R.G., di Tada, M.L., Liu, K., and Fifield, L.K., 1999, Shock melting of the Canyon Diablo impactor: Constraints from Nickel-59 contents and numerical modeling: Science, v. 285, p. 85–88, doi: 10.1126/SCIENCE.285.5424.85.

Scott, E.R.D., 1972, Chemical fractionation in iron meteorites and its interpretation: Geochimica et Cosmochimica Acta, v. 36, p. 1205–1236, doi: 10.1016/0016-7037(72)90046-4.

Scott, E.R.D., Haack, H., and McCoy, T.J., 1996, Core crystallization and silicate-metal mixing in the parent body of the IVA iron and stony-iron meteorites: Geochimica et Cosmochimica Acta, v. 60, p. 1615–1631, doi: 10.1016/0016-7037(96)00031-2.

See, T.H., Hörz, F., Mittlefehldt, D.W., Varley, L., Mertzman, S., and Roddy, D., 2002, Major element analyses of the target rocks at Meteor Crater, Arizona: NASA/TM-2002-210787, 23 p.

Shoemaker, E.M., 1963, Impact mechanics at Meteor Crater, Arizona, *in* Middlehurst, B.M., and Kuiper, G. P., eds., The Moon, Meteorites, and Comets: Chicago, Illinois, University of Chicago Press, p. 301–336.

Shoemaker, E.M., 1987, Meteor Crater, Arizona, *in* Beus, S.S., ed., Rocky Mountain Section of the Geological Society of America Centennial Field Guide: Boulder, Colorado, Geological Society of America, v. 2, p. 399–404.

Simonds, C.H., Floran, R.J., McGee, P.E., Phinney, W.C., and Warner, J.L., 1978, Petrogenesis of melt rocks, Manicouagan, impact structure, Quebec: Journal of Geophysical Research, v. 83, p. 2773–2788.

Stöffler, D., Keil, K., and Scott, E.R.D., 1991, Shock metamorphism of ordinary chondrites: Geochimica et Cosmochimica Acta, v. 55, p. 3845–3867, doi: 10.1016/0016-7037(91)90078-J.

Wasson, J.T., and Kimberlin, J., 1967, The chemical classification of iron meteorites, II: Irons and pallasites with germanium concentrations between 8 and 100 ppm: Geochimica et Cosmochimica Acta, v. 31, p. 2065–2093, doi: 10.1016/0016-7037(67)90143-3.

Wasson, J.T., and Ouyang, X., 1990, Compositional range in the Canyon Diablo meteoroid: Geochimica et Cosmochimica Acta, v. 54, p. 3175–3183, doi: 10.1016/0016-7037(90)90132-5.

Wasson, J.T., and Richardson, J.W., 2001, Fractionation trends among IVA meteorites: Contrasts with IIIAB trends: Geochimica et Cosmochimica Acta, v. 65, p. 951–970, doi: 10.1016/S0016-7037(00)00597-4.

Xue, S., Herzog, G.F., Hall, G.S., Klein, J., Middleton, R., and Juenemann, D., 1995, Stable nickel isotopes and cosmogenic beryllium-10 and aluminum-26 in metallic spheroids from Meteor Crater, Arizona: Meteoritics, v. 30, p. 303–310.

Manuscript Accepted by the Society 9 August 2004